Verdampfung von metallischen Probekörpern in Hoch-Leistungs-Plasmaströmungen

The study of evaporation of metal specimen in high energy plasma flows

Master thesis of
cand. aer. Jens Schmidt
IRS-17-S-051

Supervisor:
Priv.-Doz. Dr.-Ing. Georg Herdrich
Dr. Michael Kazeev

Institut für Raumfahrtsysteme, Universität Stuttgart
National Research Center "Kurchatov Institute", Moscow
June 2017

Contents

Kurzfassung

Bis zum jetzigen Zeitpunkt existieren keine Untersuchungen der Verdampfung von Wolfram bei Temperaturen über dem Schmelzpunkt. Daher wird in dieser Arbeit die Verdampfung von Stahl- und Wolfram-Proben wird mit Hilfe experimenteller sowie einfacher numerischer Verfahren untersucht. Zur experimentellen Bestimmung der Verdampfung wird eine ablative gepulste Plasma-Quelle (ablative pulsed plasma thruster - APPT) benutzt, um kurzzeitig sehr hohe Wärmeströme zu erzeugen. Für verschiedene Wärmeströme wurden die Temperaturänderung sowie die verdampfte Masse gemessen. Ebenso wurden die Proben mit Hilfe von optischer und Elektronen-Raster-Mikroskopie untersucht. Um Aufschluss über die Qualität verschiedener 1-D Modelle zu erhalten, wurde die Verdampfung im weiteren Verlauf der Arbeit mit Hilfe eines Finite-Differenzen-Verfahrens untersucht. Die 3 Modelle basieren dabei auf der kinetischen Gastheorie, einem semi-empirischen Ansatz und der Betrachtung als eindimensionales Stefan-Problem. Alle Modelle für Wolfram lieferten für Wärmeströme unter $115,5$ MW/cm^2 befriedigende Ergebnisse, für höhere Wärmestrome ergaben sich allerdings deutliche Abweichungen zwischen Experiment und Simulation. Durch Beobachtungen aus der Mikroskopie ergibt sich daher die Vermutung, dass ein zusätzlicher Beitrag zur Verdampfung bei hohen Wärmeströmen eine Rolle spielt. Dies kann ein konvektiver Term aufgrund des sehr hohen Temperaturgradienten innerhalb der flüssigen Phase sein. Ebenso können Gitterinstabilitäten im Wolframkristall bei hohen Temperaturen eine Rolle spielen. Die Untersuchung dieser Effekte motiviert weitere Arbeiten auf diesem Gebiet der Materialwissenschaften.

Abstract

Until today, the evaporation of tungsten at temperatures over its melting point has not been examined in experiments. Therefore, the evaporation of steel and tungsten is examined using experimental measurements and simple numerical methods within this work. A high power ablative pulsed plasma thruster (APPT) was used to apply high thermal loads onto steel and tungsten specimen. Also the temperature change and evaporated mass for different loads were measured. In addition, selected samples were also examined by optical and electron microscopy. Furthermore, the evaporation was also simulated with finite differences by the use of three different 1-D evaporation models: one based on the kinetic gas theory, one semi-empirical model and by consideration as a one dimensional Stefan problem. All models generated good results for heat fluxes lower than 115.5 MW/cm^2, but the evaporated mass differs for higher thermal loads. Due to these results and the microscopical observations, it is assumed that additional effects contribute to the evaporation at very high energies. Additional effects may be a convective mass transport in the liquid layer of the sample due to the high temperature gradient. Also instabilities of the tungsten crystal lattice may lead to faster progress of the liquid phase in the sample. The investigation of the influences, especially of the convective term motivates intensified research of these influences in this area of material science.

Nomenclature

Symbol	Name
A	Area [m^2]
$\vec{B}$	Magnetic flux density [T]
C	Capacity [F]
d	Diameter [m]
E	Energy [J]
F	Lorentz Force [N]
f	Freguency [s^{-1}]
E_s	Lattice energy [eV/ atom]
H	Heat [J]
I	Electric Current [A]
$\vec{j}$	Electric flux density [$\mathrm{A/ms}^2$]
L	Inductance [H]
l	Length [m]
L_v	Latent heat of vaporization [$\mathrm{kJ\,mol}^{-1}$]
L_m	Latent heat of melting [$\mathrm{kJ\,mol}^{-1}$]
Ma	Mach-Number [-]
M	Molar mass [$\mathrm{kg\,mol}^{-1}$]
m	Mass [kg]
Nu	Nusselt number [-]
P	Power [W]
Q	Electric charge [J]
R	Resistance [Ω]
R_s	Specific gas constant [$\mathrm{J\,kg}^{-1}\,\mathrm{K}$]
$\dot{q}$	Heat flux [$\mathrm{W/m}^2$]
T	Temperature [K]
t	Time [s]
U	Voltage [V]
V	Voltage [V]
v	velocity [$\mathrm{m\,s}^{-1}$]
z	Spatial dimension [m]
α	Thermal diffusivity [$\mathrm{m}^2\mathrm{s}$]
ρ	Density [$\mathrm{kg/m}^3$]
λ	Heat conductivity [$\mathrm{W\,m}^{-1}\,\mathrm{K}$]
η	Efficiency [-]
ω	Frequency [$1\mathrm{s}^{-1}$]

Constants

$e_0 = 1.602 \cdot 10^{-19}$ C $= 4,8 \cdot 10^{-10}$ Fr	Elemental charge
$E_{e,Fe}$ eV	Energy of the first excited state of iron
$E_{e,W}$ eV	Energy of the first excited state of tungsten
$E_{i,Fe} = 17.42$ eV	First Ionization energy of iron
$E_{i,W} = 7.86$ eV	First Ionization energy of tungsten
$k = 1.38062 \cdot 10^{-23}$ J K^{-1}	Boltzmann constant
$h = 6.626 \cdot 10^{-34}$ J s	Planck constant
$m_{a,Fe} = 9.2733 \cdot 10^{-26}$ kg	Atomic mass of iron
$m_{a,W} = 3.0527 \cdot 10^{-25}$ kg	Atomic mass of tungsten
$M_{Fe} = 55.85$ g mol^{-1}	Molar mass of iron
$M_W = 183.84$ g mol^{-1}	Molar mass of tungsten
$N_A = 6.022140 \cdot 10^{23}$ mol^{-1}	Avogadro Constant
$\epsilon_0 = \frac{1}{\mu_0 c^2} = 8.854187 \cdot 10^{-12}$ F m^{-1}	Vacuum permittivity
$\mu_0 = 4\pi \cdot 10^{-7}$ H m^{-1}	Magnetic field constant
$\pi = 3.14159$	Mathematical constant
$\sigma = 5.670367 * 10^-8$ W/m^{2}K^4	Stefan-Boltzmann-constant
$T = \frac{e}{k} \cdot E = \frac{1{,}602 \cdot 10^{-19}\text{C} \cdot 1\text{eV}}{1{,}381 \cdot 10^{-23}\text{J/K}} = 11600$ K	Electron temperature in Kelvin for 1 electron volt

Indices

b	propellant
c	capacitor
evap	evaporation
i	Matrix index
j	Matrix index
l	liquid
v	Vapour
m	Molten
p	propellant
rad	radiation
s	solid

Abbreviations

APPT	Ablative Pulsed Plasma Thruster
CFL	Courant-Fourier-Levy
KH	Knudsen-Hertz formula
SE	Semi-Empirical formula
PPT	Pulsed Plasma Thruster
PTFE	Polytetrafluorethylen

1 Introduction

Knowledge of the processes of metal evaporation and sublimation is fundamental for the understanding of high-temperature behavior of metals. In science and technology, there are many applications for metals at high temperature, especially tungsten. Obvious examples are materials used in re-entry of space of vehicles, electrode material in plasma facilities, plasma-facing walls in thermonuclear fusion devices and many others. In this temperature regions, tungsten is often used as it is the only material feasible, having a melting point of 3965 K and a boiling point around 6203 K [1–3]. Due to high thermal loads that can be expected espcially in thermonuclear fusion devices, evaporation of the upper layer of the material arises. This process of sublimation and evaporation is not fully understood for temperatures above the melting (and boiling) point of tungsten. Nonetheless, in the last years, no further attempts to examine the high temperature effects in tungsten have been taken, mainly because it is mostly used as a high temperature material in temperature regions below the melting point. Still, the investigation of the behavior of high-temperature materials heated to temperatures close to their thermal degradation temperature has more than a century [4] of history. Originally, this research was motivated by the need to determine the resistance of a tungsten filament light bulb, which is the principal determinant of its service life. The main interest and the possibility of the experiment were significantly lower than the temperature of the melting point, resulting in a relatively low rate of sublimation. In [4–6], the temperatures do not exceed 3200 K. When exceeding these temperatures, processes on the surface layer of metallic specimen are of interest. To obtain a more sophisticated model for the surface, the plasma flow interaction with metallic specimen consisting of stainless steel and tungsten is examined within this work. In comparison to the work of Langmuir [4], there are new possibilities for investigating the behavior of high-temperature materials through the development of high-power plasma-generators. To achieve high temperatures and energy fluxes, a facility with an instationary plasma source is used.

Ablative pulsed plasma thrusters (APPT), also known as instationary magneto-plasma-dynamic (iMPD) thrusters, have been known for more than 50 years [7] in the application as low thrust engines for space applications with need of high specific impulse. They were largely used for purposes of attitude control and house-keeping of satellites and space probes e.g. Zond 2 [8]. Although their usefullness in electric propulsion was demonstrated, other applications seem feasible. While the operation of stationary plasma coating facilities is very common, the use of instationary plasma sources has yet some challenges. Nonetheless it provides a (relatively) low priced alternative while giving the possibility to work at high energies and temperatures that are highly complicated to realize with stationary plasma facilities.

An experimental facility based on an APPT is thus used to examine the interaction of metal specimen with a high energy pulsed plasma flow and the evaporated mass and the absorbed heat of the samples are measured. The experimental method used can be called "thermal ablation" due to similarities to electron beam or laser ablation, but achieving higher heat fluxes on greater areas for short time. Regarding the challenges, due to the instationary process, many assumptions that have validity for stationary plasma generators have to be revisited.

Furthermore, a numerical simulation of the evaporation, heat conduction and heat flux in the sample is carried out. In context of this simulation, a kinetic model for evaporation of steel is used and validated. Afterwards, the model is adapted for tungsten, which has the same modification of the crystal lattice. Nonetheless, due to different effects occurring at the evaporation of tungsten, the model has to be enhanced and refined to resemble the processes of the evaporation correctly. This leads to the possibility to determine the evaporation temperature of tungsten and to numerically study the high temperature behaviour of tungsten. In addition, the evaporation process can be analyzed further. This analysis can also be assisted by examination of the specimen with optical and electron microscopy, leading to deeper knowledge about the degradation of the surface. With this information, the durability of the material can be estimated, leading to insights for current and future applications of tungsten in high temperature environments. All experiments have been carried out at the APPT experimental facility at the National Research Center "Kurchatov Institute" in Moscow.

2 Description of the experimental facility

To measure the evaporation of the metallic specimen, the former mentioned Ablative Pulsed Plasma Thruster (APPT) experimental facility is used. The facility consists of a pulsed power supply, an low inductive feeder with a cable bridge, the plasma source and furthermore the vacuum system. A picture of the facility can be seen in figure 1. The power supply is made of capacitor banks with different capacities and maximal charging voltages that are connected as required. The feeder is connected to the capacitor bank using 48 high current coaxial cables with a total inductance of $3 \cdot 10^{-9}$ H. The rectangular vacuum chamber is 3 m long and has an total volume of 1.2 m^3. A vacuum with a pressure of 10^{-4} Torr with an evacuation volume flow of 5000 $L\,s^{-1}$ is sustained by fore-vacuum and diffusion pumps.

2.1 Plasma source

The plasma source consists of a coaxial APPT and has a length of 9 cm. A scheme of the geometry can be seen in Figure 2. It is based on a cylindrical copper anode (3) with a diameter of $d_a = 10$ cm and a inner tungsten cathode (1) with a diameter of $d_c = 2$ cm. These electrodes are insulated by Polytetrafluorethylen (PTFE) as an insulator (2) and also as ablated propellant fed into the vacuum through the vacuum feeder, which has an inductance of 10^{-8} H. The high current discharge is triggered by a low power breakdown plasma, which is moving through the holes of the inner electrode to the outer electrode. The breakdown voltage for Teflon as insulator amounts 22 kV/cm, which limits the maximal charging voltage of the facility, although other materials can be used. To generate an quasi-steady plasma flow, the facility is operated with

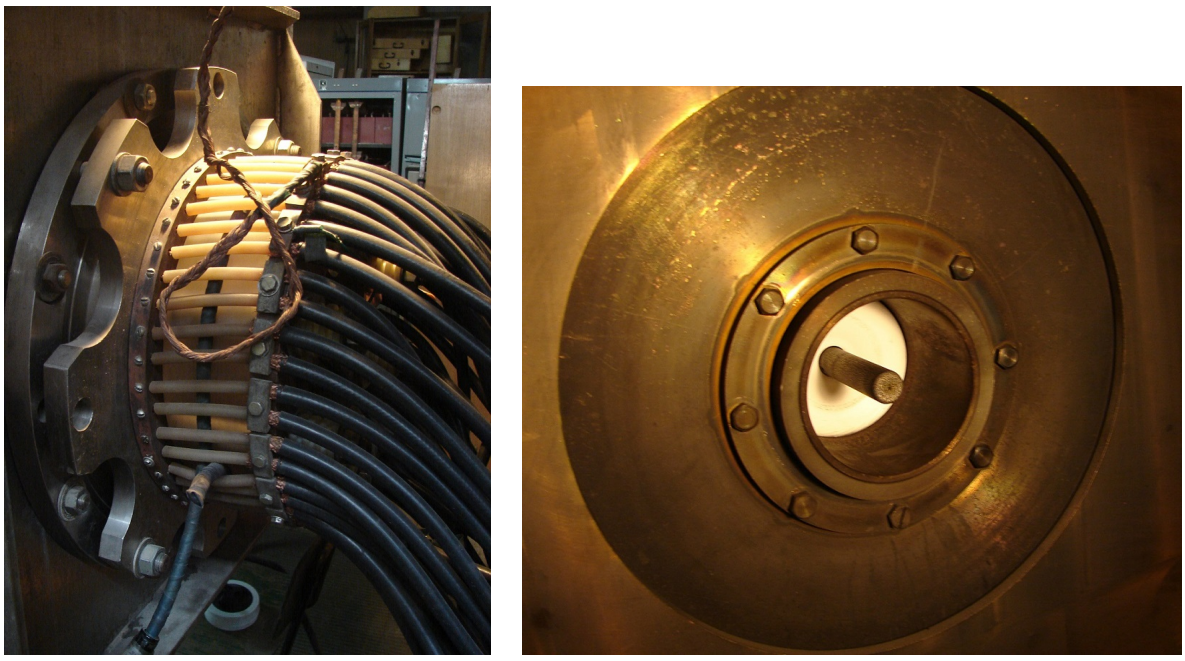

(a) Power supply with Rogowski Coil

(b) Plasma generator

Figure 1: Images of the APPT facility

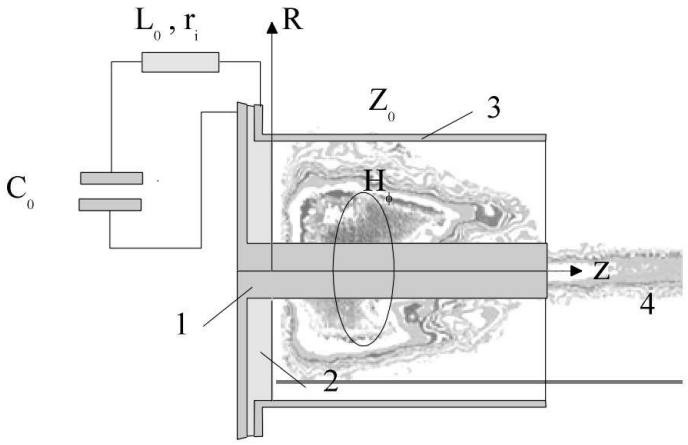

Figure 2: Schematic of the PPT with tungsten cathode (1), teflon propellant insulator (2), copper anode(3) and plasma flow (4)

discharge pulses having a duration between 10 µs up to a few milliseconds [9]. At maximum current, the source is connected to another capacitor bank by a high current switch. In this way, an wide area of discharge currents as well as long discharge times could be achieved.

2.2 Diagnostics

The facility provides different diagnostics for plasma measurements. The discharge current can be measured with an Rogowski coil, which function is described further in chapter 4.1. Voltage is measured at the capacitor bank by capacitive voltage dividers. With a high-speed camera, photography of the discharge is possible with a maximal resolution in time of $2 \cdot 10^{-8}$ s. An image of the facility during operation can be seen in figure 3. The energy flux to the propellant can be measured with a small sized thermistor which stores the integral heat flux leading to a measurable temperature change behind the sample. [10]. Temperature of the metallic specimen can also be measured with a resistance thermo-element.

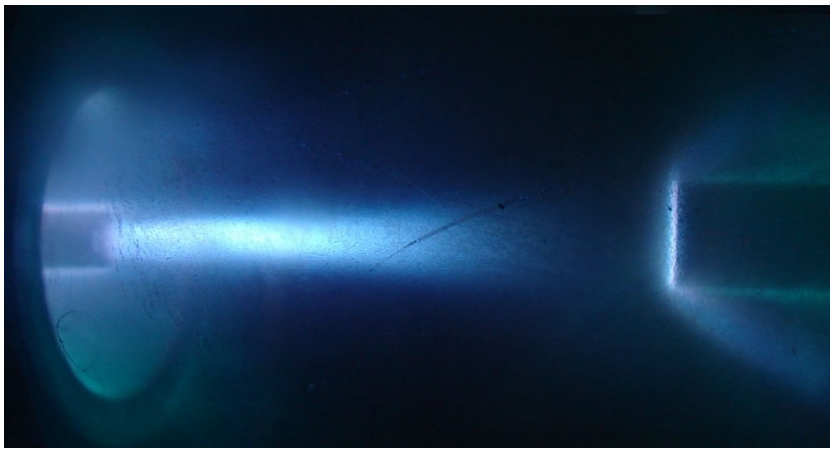

Figure 3: Plasma source with specimen during operation

3 Fundamentals

3.1 Pulsed Plasma Thrusters

The use of pulsed plasma thrusters can be found as early as in 1934 in Russia [7]. The first space-qualified pulsed plasma thruster was launched in 1960 onboard of the Zond-2 spacecraft. Since this time, the fundamental technology behind pulsed plasma thrusters has not changed. A plasma is generated between two electrodes and propellant mass is ablated by the arc discharge. Due to the current $\vec{j}$ in the plasma, a magnetic field $\vec{B}$ arises, leading to a Lorentz-force $F = \vec{j} \times \vec{B}$ that accelerates the plasma. Within the thruster, energy is mainly lost due to dissociation, ionisation of the propellant and plasma radiation. Basically, at the APPT facility, there are two modes of acceleration:

- Electrothermal, where the propellant is mainly accelerated by the gas dynamic expansion due to the heat coupled into it.
- Electrodynamic, in which acceleration is mainly given by the magnetoplasmadynamic effects trough the Lorentz-force.

For the APPT facility as for pulsed plasma thrusters in general, the electrodynamic mode mainly takes place at high discharge voltages above 5 kV. At lower discharge voltages, the discharge current is not high enough to produce an sufficient magnetic field.

3.2 Slug-shot model

To calculate the plasma velocity, the slug-shot model introduced in [11–13] is used. It is a electro-mechanical 1-D model with simplifications, but it can be used to derive some essential information about the plasma source. We assume the whole momentum is given by the Lorentz-Force and that the whole propellant is ablated in one pulse. The relation between the acceleration $\ddot{z}$ of the ablated propellant and the change of the electrical charge $\dot{Q}$ is given by the differential equation

$$m_b \ddot{z} - \frac{1}{2} L' \dot{Q}^2 = 0, \tag{3.1}$$

whereof the change of inductance for coaxial thrusters can be assumed as $L' = const.$ The ablated propellant mass m_b can be described by the empirically derived equation

$$m_b = 1.32 \cdot 10^{-6} A_p^{0.65} E_0^{0.35}, \tag{3.2}$$

in which A_p is the propellant surface exposed to the plasma and E_0 is the initial capacitor energy [12, 13]. It has to be considered, that the velocity distribution in the plasma is very broad, so that a plasma velocity calculated by this model may not represent the velocity of the whole ablated mass.

3.3 Evaporation

Under vacuum, evaporation of atoms from the surface of solids and liquids can occur in dependence of the remaining pressure and surface temperature of the heated material.[14–16]. In detail, the heat flux first leads to liquification of the material, followed by sublimation and evaporation at the interface between liquid and gas phase. In front of the material, a thermal skin layer with the thickness $\delta_{th} = (\alpha\tau)^{0.5}$ is formed. After evaporation, the vapour is removed by the plasma flow, although still evaporation in a considerably smaller rate from the liquid phase is taking action. A detailed description of the assumptions and the modeling of the evaporation can be found in chapter 6.

3.4 Crystal bonding

In transitions metals as iron (Fe) and tungsten (W), the metallic bonding is more close to the covalent bonding, leading to a relatively high binding energy for $E_s = 4.29$ eV/ atom for iron and $E_s = 8.66$ eV/ atom for tungsten. The typical modification of their crystalline structure is body-centered cubic (bcc). For steel modifications to other crystalline structures occur at high temperatures, changing some thermodynamical properties drastically, especially the heat capacity. This is not the case for tungsten, which only has a meta-stable β phase, but normally exclusively appears in its α phase with a lattice constant of 316 pm.

3.5 Finite Difference Scheme

For the numerical solution of partial differential equations, these equations are discretized with different scheme. Within this work, a finite difference scheme is used in which the differentiations are approximated by differences [17]. For a scheme of second order, following approximations are used:

$$T_t = \frac{1}{\Delta t}(T_{i+1,j} - T_{i,j}) \tag{3.3}$$

with the step size in time Δt. The second derivation in space is approximated by

$$T_{zz} = \frac{1}{\Delta z^2}(T_{i,j+1} - 2T_{i,j} + T_{i,j-1}) \tag{3.4}$$

with the finite difference in space Δz. The one-sided backward differentiation quotient in space is given by

$$T_z = \frac{1}{\Delta z}(T_{i,j} - T_{i,j-1}) \tag{3.5}$$

Using a direct numerical calculation method, the CFL-condition has to be fulfilled:

$$\mathrm{CFL} = \frac{\Delta z^2 \alpha}{\Delta t} \leq 0.5 \tag{3.6}$$

with the thermal diffusivity α. Due to this condition, for short time periods and small spacial steps, very small values for Δz are required, leading to small values for Δt and thus to the need of very fine grids, which increases calculation time.

4 Characteristics of the electrical discharge

To verify the electric discharge in the plasma source, the electric current during a discharge pulse with a duration of 10-90 µs is measured. After calculating current and voltage at the power supply, the energy transferred to the plasma can be measured.

4.1 Measurement of the current with a Rogowski Coil

For the measurements of the discharge current, a Rogowski coil is used [18]. It consists of a coil with n windings, that is wrapped around the cable bridge, as seen in Figure 4a) [19]. With this installation, the current can be measured relatively independent to the discharge conditions. The Rogowski coil is a flux-to-voltage transducer that consists of an helical coil cored by an 10 mm placstic rod placed around the probed conductor. A picture of the coil can be found in Figure 1a), a schematic of the coil is also shown in Figure 4a). It has the capability of measuring very low to very high currents (in between 1 mA and 2 MA). The electrical circuit is schemed in Figure 4b). Due to the inductance of the coil, the methodical error ascends over time, as there can be a difference up to 10% between the measured current at the coil $I_1(t) = V_{measured}(t)/R_{sh}$ and the real current $I(t)$ in the conductor. The relation between both currents is given by the differential equation

$$M\frac{dI}{dt} = L\frac{dI_1}{dt} + I_1 R, \tag{4.1}$$

where t is the time and R is the resistance of the Rogowski coil, calculated by $R = R_{sh} + r$, where r is the active resistance and R_{sh} is the shunt resistance. Integration of Formula 4.1 leads to the following expression for the current in the conductor:

$$I(t) = -\frac{L}{M}\left[I_1(t) + \frac{R}{L}\int_0^t I_1(t)dt\right] \tag{4.2}$$

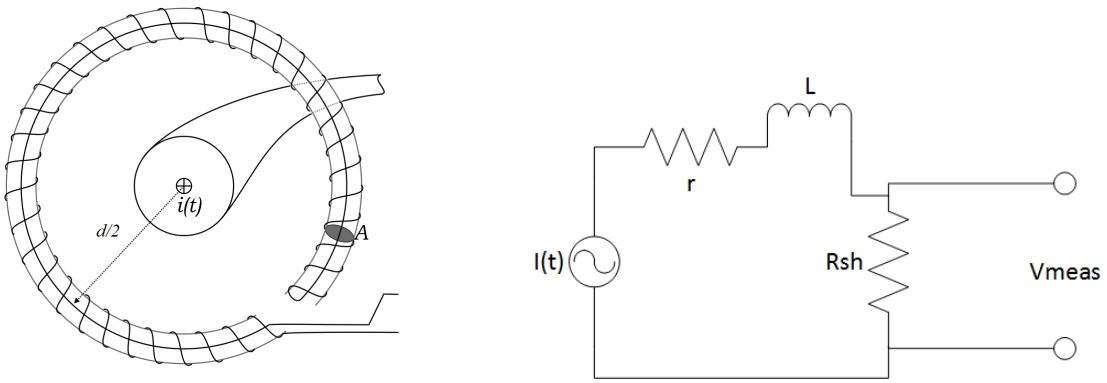

(a) Illustration of the coil

(b) Equivalent circuit

Figure 4: Representation of the Rogowski coil

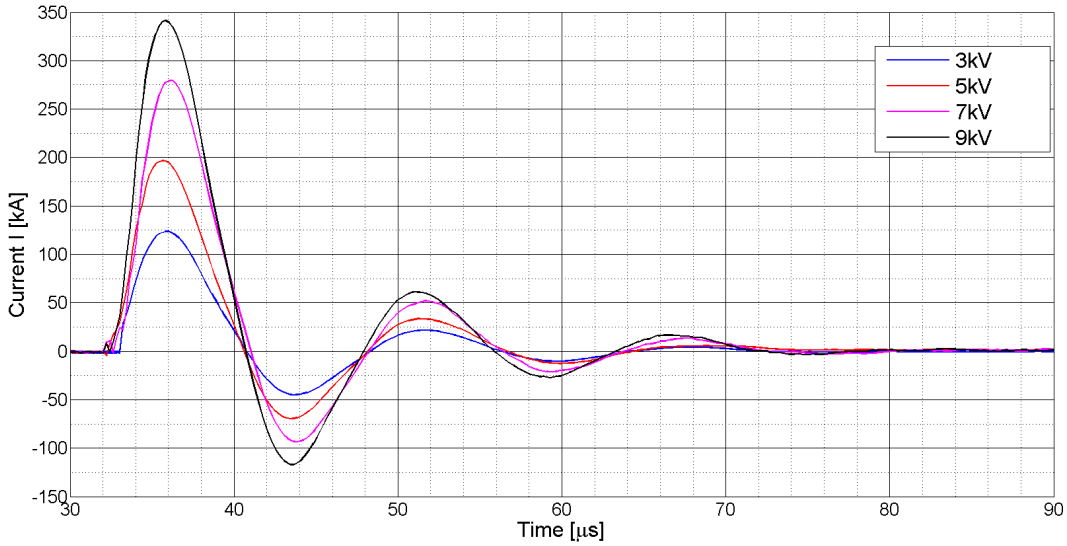

Figure 5: Measured current of the Rogowski Coil

With numerical integration of the signal $I_1(t)$ after the measurement, the real current $I(t)$ can be calculated. The intrinsic inductance of the Rogoski coil can be calculated by

$$L = \frac{\pi^2 n^2 D^2}{l} \tag{4.3}$$

and mutual resistance by

$$M = \frac{\pi^2 n D^2}{l} \tag{4.4}$$

This leads to $\frac{L}{M} = n$. To keep the shunt resistance relatively inductance-free, which can be satisfied by the condition $R_{sh} \leq 5\omega L_{sh}$, the resistor is made of metallic foil strips, that are crossed and separated in each other. The given resistor with the parameters $a = 5$ cm, $b = 5$ cm and $h = 0.2$ mm has an intrinsic inductance of $L_{sh} = \mu_0 \frac{ah}{b} = 1.25$ nH which leads to $\omega L_{sh} = 0.37$ mΩ.

4.2 Results of the measurement

The discharge current was measured for capacitors with an capacity of $C = 144$ µF. The used Rogowski coil consisted of $n = 995$ windings with an inner diameter of $d = 0.001$ m and had an length $l = 1.105$ m. Measurements were done with the capacitor bank charged to initial voltages U_0 of 3, 5, 7 and 9 kV. The active resistance of the coil was $r = 0.792$ Ω and an inductance of $L = 58.66$ µH for 1 kHz, $L = 58.33$ µH for 10 kHz and $L = 54.47$ µH for 100 kHz was measured. The shunt resistance was $R_{sh} = 0.05 \pm 0.005$ Ω. The measured currents for the different voltage charges can be seen in figure 5. As it can be seen, the amplitudes of the current grows with ascending U_0. If the circuit of the connected capacitor and the device is assumed as an harmonic

U_0 [kV]	$C \cdot U_0$ [A s]	$\lvert \int_{t=0}^{t=t_end} I(t)dt \rvert$ [A s]	E_{cap} [kJ]	$E(t_end)$ [kJ]
3	0.4320	0.4480	0.648	0.636
5	0.72	0.7569	1.8	2.1783
7	1.01	1.0941	3.528	3.8114
9	1.296	1.3368	5.823	6.3245

Table 1: Comparison of analytically and mean integral calculated charge and energy

oscillator, the voltage at the device can be calculated via

$$U_e(t) = R * I(t) + U_c(t) + L_{circuit} \cdot \frac{dI(t)}{dt}, \tag{4.5}$$

where R can be assumed as negligible. The charge of the capacitor is related to the current via:

$$I = \frac{dQ}{dt} = C \cdot \frac{dU}{dt} \tag{4.6}$$

Integration with the border $[0, t]$ leads to

$$U_c(t) = U_0 + \frac{1}{C} \int_0^t I(t)dt. \tag{4.7}$$

This leads to the assumption, that at the end of the discharge, the integral of the current has to be equal to the initial charge $C \cdot U_0$. Comparisons for the results shown in Figure 5 can be read in table 1. The differences can be explained by errors in the measurement and caused by the interpolation of the measurement data. Via the relation $P(t) = U(t) \cdot I(t)$, the power transferred to the discharge can be calculated, leading to the results shown in Figure 7. Integration of the power leads by $E(t) = \int_{t=0}^{t} P(t)dt$ to the energy, displayed in Figure 6. Also displayed is the initially stored energy in the condensator bank, calculated by

$$E_{cap} = \frac{CU_0^2}{2}. \tag{4.8}$$

The discrepancies can be explained by uncertainties in the measurement of the charging voltage and energy stored in the magnetic field created by the overall inductance. These may be corrected by new estimations for the inductance. An Fast-Fourier-Transformation of the original measurement signal has been done, leading to an frequency $f_0 = 5.8937 \cdot 10^4$ s^{-1} of the circuit. Via the relation

$$f_0 = \frac{1}{2\pi\sqrt{LC}} \tag{4.9}$$

the theoretical inductance of the circuit can be calculated, leading to $L_{meas} = 5.0641 \cdot 10^{-8}$ H, which is in good agreement with the assumed inductance of the vacuum feeder.

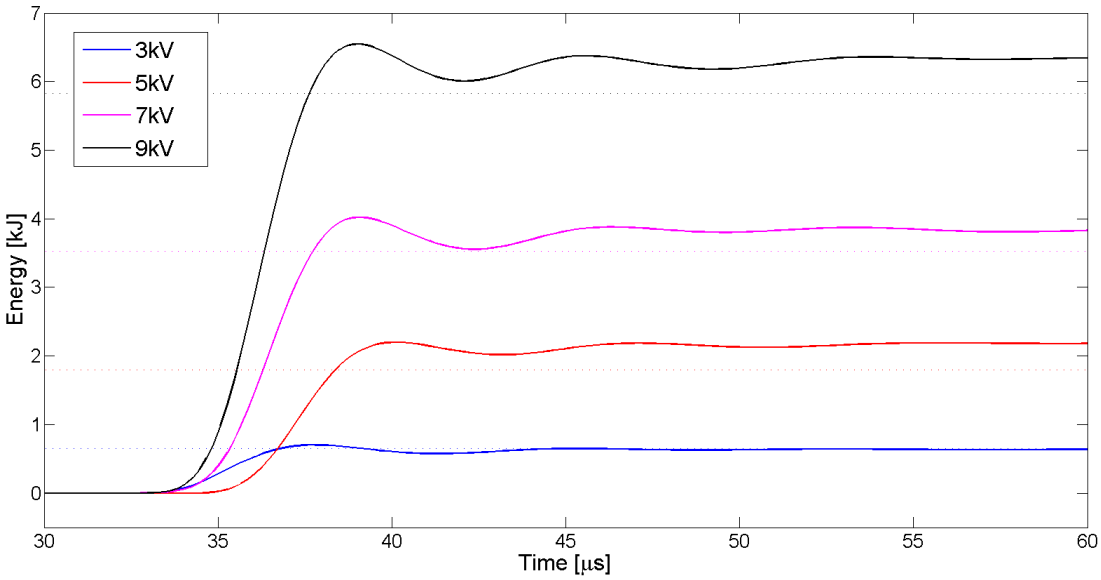

Figure 6: Calculated energy input (continuous lines) at the plasma source and initially stored energy of the condensator bank (dotted)

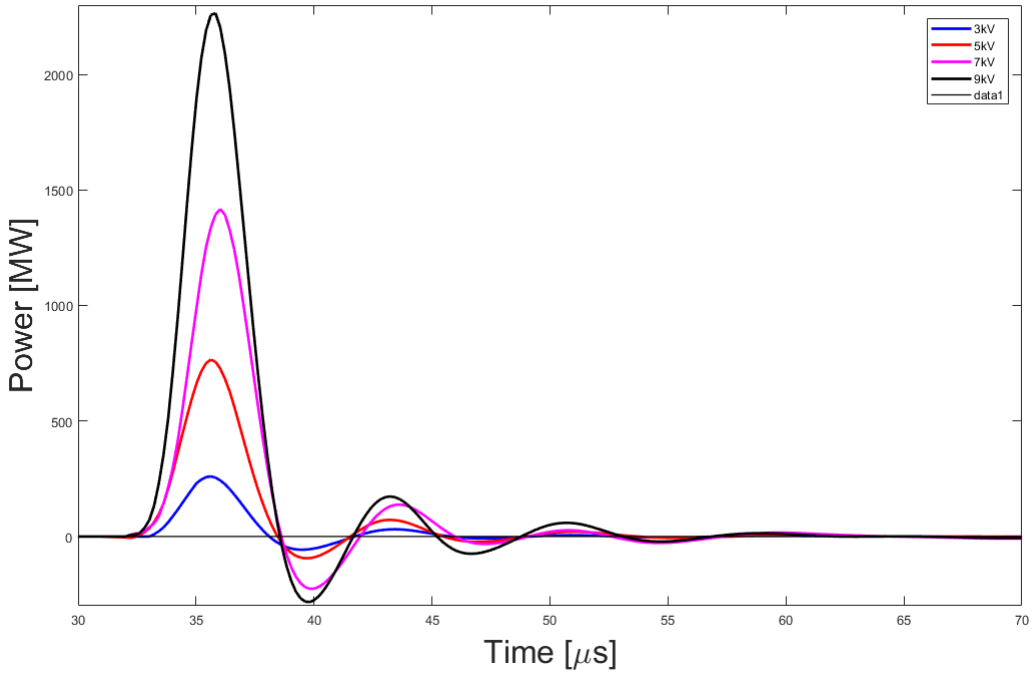

Figure 7: Calculated power input at the plasma source

U_0 [kV]	3	5	7	9
$E_{0,\eta}$ [J]	$6.48 \cdot 10^2$	$1.8 \cdot 10^3$	$3.528 \cdot 10^3$	$15.832 \cdot 10^3$
$m_{b,empiric}$ [kg]	$5.307 \cdot 10^{-7}$	$7.59 \cdot 10^{-7}$	$9.604 \cdot 10^{-7}$	$1.145 \cdot 10^{-6}$
m_b [mol]	$5.307 \cdot 10^{-6}$	$7.59 \cdot 10^{-6}$	$9.604 \cdot 10^{-6}$	$1.145 \cdot 10^{-5}$
$v = \dot{z}$ [km/s]	27.3186	53.0472	82.37	112.94
E_{diss,C_2F_4} [J]	0.185	2.64	3.351	4

Table 2: Calculated values for plasma speed and ablated mass, empirical formula

$m_{b,appt}$ [kg]	$1.296 \cdot 10^{-7}$	$3.6 \cdot 10^{-7}$	$7.056 \cdot 10^{-7}$	$1.1664 \cdot 10^{-6}$
$m_{b,appt}$ [mol]	$1.296 \cdot 10^{-6}$	$3.6 \cdot 10^{-6}$	$7.056 \cdot 10^{-6}$	$1.1664 \cdot 10^{-5}$
$v = \dot{z}$ [km/s]	111.86	111.84	112.12	110.8711
E_{diss,C_2F_4} [J]	0.452	1.257	2.463	4.1

Table 3: Calculated values for plasma speed and ablated mass with $m_b = 0.2\ \mu\mathrm{g\,J^{-1}}$

4.3 Calculation of the plasma source characteristics

The slug model introduced in chapter 3.2 is used to calculate the characteristics of the plasma source in a simplified manner. To determine the ablated mass, the empirical relation 3.2 from [11, 12] is used with an ablated area $A_p = 7.54982 \cdot 10^{-3}$ m^2. Furthermore the ablated mass was calculated with an assumption of $m_b = 0.2\ \mu\mathrm{g\,J^{-1}}$. Also, the ablated mass in molar units is calculated, using the molecular weight of PTFE $M_{C_2F_4} = 100.02\ \mathrm{g\,mol^{-1}}$. The energy for full dissociation of PTFE is $E_{diss,C_2F_4} = 349.1\ \mathrm{kJ\,mol^{-1}}$, leading to the energy lost due to dissociation E_{diss,C_2F_4}, which is very low in comparison to the bank energy. For a cylindrical plasma source, the change of inductance can be calculated as

$$L' = \frac{\mu_0}{4} \frac{d_a^2 - d_i^2}{d_a} = 2.897 \cdot 10^{-8}\mathrm{H}. \tag{4.10}$$

Using these values, the equation 3.1 can be formed and integrated to

$$v(t) = z\dot{(t)} = \int_0^t z\ddot{(t)}dt = \frac{1}{2m_b} L' \int_0^t \dot{Q}^2 dt, \tag{4.11}$$

by which the maximal plasma velocity $v(t)$ can be calculated. The resulting maximal plasma velocity is given in tables 2 and 3, in relation to the effective energy used for ablation $E_{0,\eta} = \eta \cdot E_0$ with $\eta = 0.4$. The results of the calculations are shown in table 2 for the empirical formula and for the linear assumption in table 3. It can be seen, that the plasma velocity v is very high, but as the dissociation energy for PTFE is quite low, the energy lost due to full dissociation is also very low in comparison to the condenser bank energy. Therefore losses from the dissociation are negligible for the incoming heat flux at the samples.

5 Interaction of the plasma flow with the specimen

In order to determine the heat flux to the sample, the temperature behind the specimen is measured. The diameter of all specimen is $d_{sample} = 0.025$ m, while the height of the steel specimen is $h_{Fe} = 0.0005$ and the height of the tungsten specimen is $h_W = 0.008$ m. The initial mass of the steel and tungsten specimen is $m_{Fe} = 1.75846$ g and $m_{Fe} = 7.96768$ g, respectively. The area of the PPT exit is $A_{PPT} = \frac{\pi}{4}(d_a^2 - d_c^2) = 0.0075$ m^2. The area of the sample exposed to the plasma flow is $A_{sample} = 4.9087 \cdot 10^{-4}$m^2. Due to surface effects, in some experiments only partial evaporation occurs. An image of the processed specimen is shown in figure 11, with the experimental results of the corresponding specimen given in the tables 4,5 for the measured evaporated mass and tables 6 and 7 for the measured temperatures.

5.1 Measurement of the evaporated mass

During the interaction of the specimen with the instationary plasma flow, mass is evaporated from the surface. The weight of the specimen is measured after a specific number n_{pulse} of pulses. Thus the evaporated mass Δm_{pulse}per pulse can be estimated. For an discharge voltage of $U_0 = 3$ kV changes in mass were to small to be measured. Furthermore, at 9 kV less pulses where used, as 3 pulses resulted in destruction of the steel specimen and temperature sensor. The obtained masses are displayed in Table 4 and 5 and displayed in combination with the measured dissipation energy in figure 8.

5.2 Measurement of the temperature and absorbed heat

In order to find the heat transferred to the sample, the temperature behind the specimen is measured. As it can be seen in figure 9 and 10, the specimen starts to cool down after reaching a maximum temperature due to heat conduction into the sample positioning assembly. It is assumed that the temperature loss due to cooling is the same whilst the temperature is rising to the maximum, leading to a higher temperature change ΔT in overall. The absorbed heat of the sample with mass m_{sample} is calculated. In respect of the heat absorbed by the temperature

Specimen	U_0 [kV]	m_1 [kg]	m_2 [kg]	Δm [kg]	n_{pulse}	Δm_{pulse}
Steel 2	5	$1.75846 \cdot 10^{-3}$	$1.75790 \cdot 10^{-3}$	$1.56 \cdot 10^{-6}$	10	$1.56 \cdot 10^{-7}$
Steel 3	7	$1.78256 \cdot 10^{-3}$	$1.77681 \cdot 10^{-3}$	$5.75 \cdot 10^{-6}$	10	$5.75 \cdot 10^{-7}$
Steel 4	9	$1.76112 \cdot 10^{-3}$	$1,75659 \cdot 10^{-3}$	$4.53 \cdot 10^{-6}$	3	$1.51 \cdot 10^{-6}$

Table 4: Evaporated mass of steel specimen

Specimen	U_0 [kV]	m_1 [kg]	m_2 [kg]	Δm [kg]	n_{pulse}	Δm_{pulse} [kg]
W 3	5	$7.96768 \cdot 10^{-3}$	$7.96693 \cdot 10^{-3}$	$7 \cdot 10^{-7}$	10	$8 \cdot 10^{-8}$
W 1	7	$7.65751 \cdot 10^{-3}$	$7.65553 \cdot 10^{-3}$	$1.98 \cdot 10^{-6}$	10	$1.98 \cdot 10^{-7}$
W 2	9	$7.63090 \cdot 10^{-3}$	$7.62549 \cdot 10^{-3}$	$5.41 \cdot 10^{-6}$	5	$1.082 \cdot 10^{-6}$

Table 5: Evaporated mass of tungsten specimen

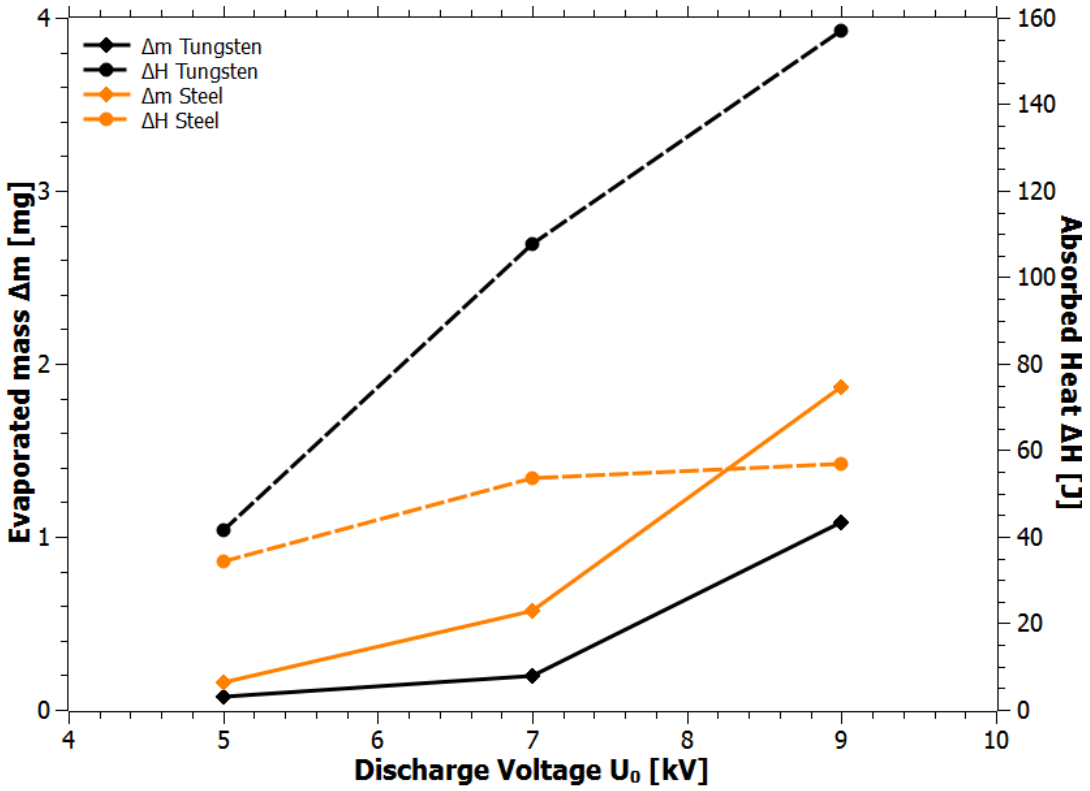

Figure 8: Measurement results for the evaporated mass Δm and absorbed heat ΔH for tungsten (black) and steel (orange)

sensor with mass $m_{sensor} = 0.16021$ g and heat capacity $c_{p,sensor} = 1670\ \mathrm{J\,kg^{-1}\,K}$ this leads to:

$$\Delta H = (c_{p,sample} m_{sample} + c_{p,sensor} m_{sensor}) \Delta T. \tag{5.1}$$

In table 6 and 7, the measured changes of the temperature are shown and the calculated absorbed heat with sensor ΔH and without the sensor H_2 are listed. Also the coefficient for the cooling $\frac{\partial T}{\partial t}$ is given.

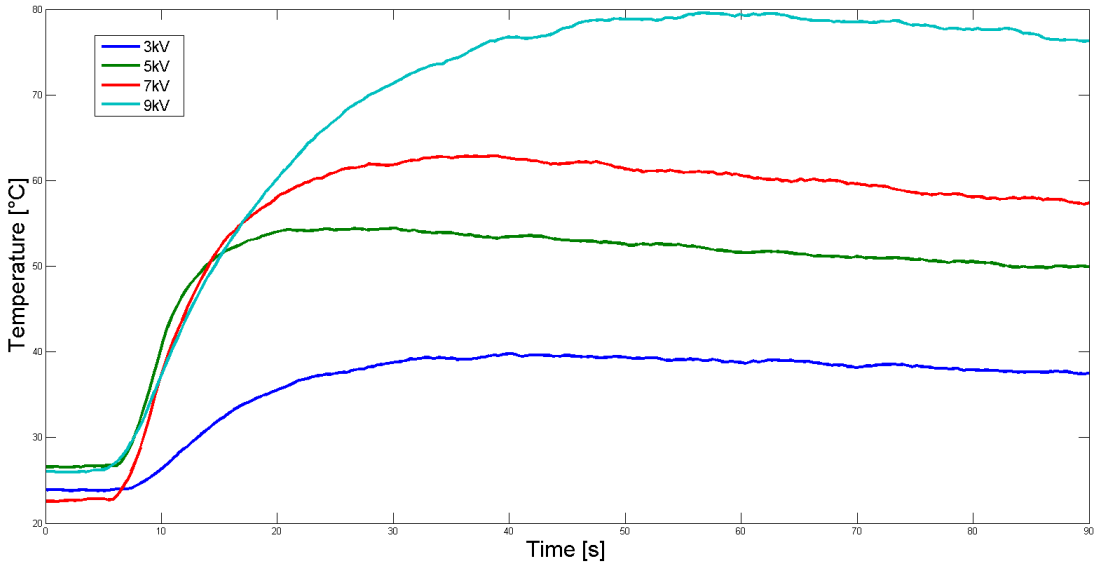

Figure 9: Temperature measurements for steel

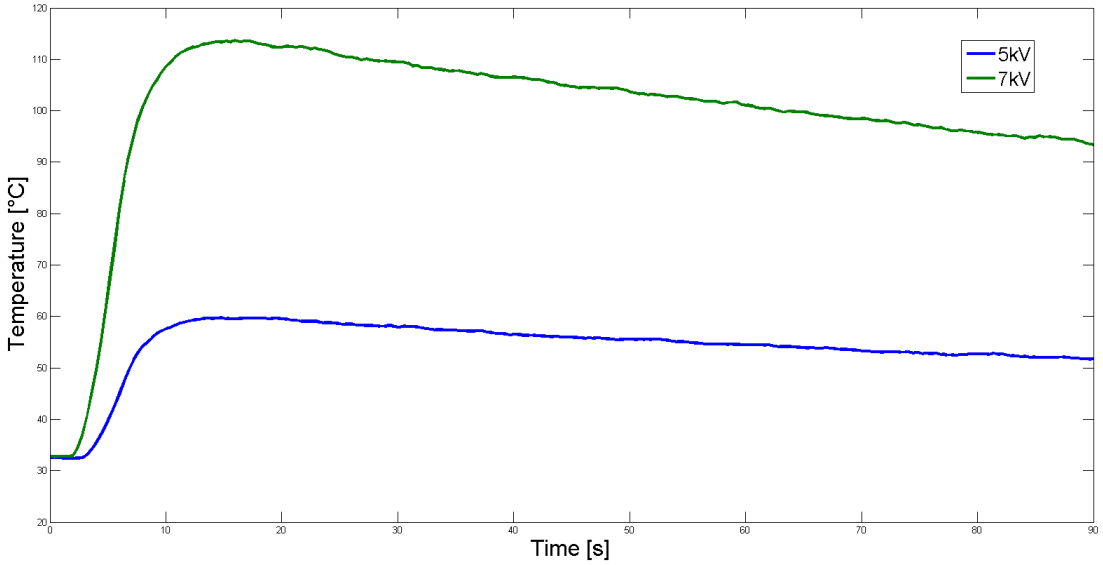

Figure 10: Temperature measurements for tungsten

Specimen	U_0 [kV]	$\Delta\bar{T}$ [K]	T_{max} [°C]	$(\frac{\partial T}{\partial t})_{cool}$ [K s^{-1}]	ΔH [J]	ΔH_2 [J]
Steel 1	3	15	40.48	-0.1616	16.719	15.1329
Steel 2	5	31.16	55.5	-0.1198	34.37	26.0428
Steel 3	7	47.92	63.6	-0.1479	53.41	37.3300
Steel 3	9	50.8	101.6	-0.1996	56.71	48.4662

Table 6: Temperature changes and absorbed heat for different charging voltages for steel

Specimen	U_0 [kV]	$\Delta\bar{T}$ [K]	T_{max} [°C]	$(\frac{\partial T}{\partial t})_{cool}$ [K s^{-1}]	ΔH [J]	ΔH_2 [J]
W 3	5	31.4	60.784	-0.1305	41.546	35.1349
W 1	7	83.9	116.0	-0.6387	107.57	94.7235
W 2	9	122.8	-	-	157.017	-

Table 7: Temperature changes and absorbed heat for different charging voltages for tungsten

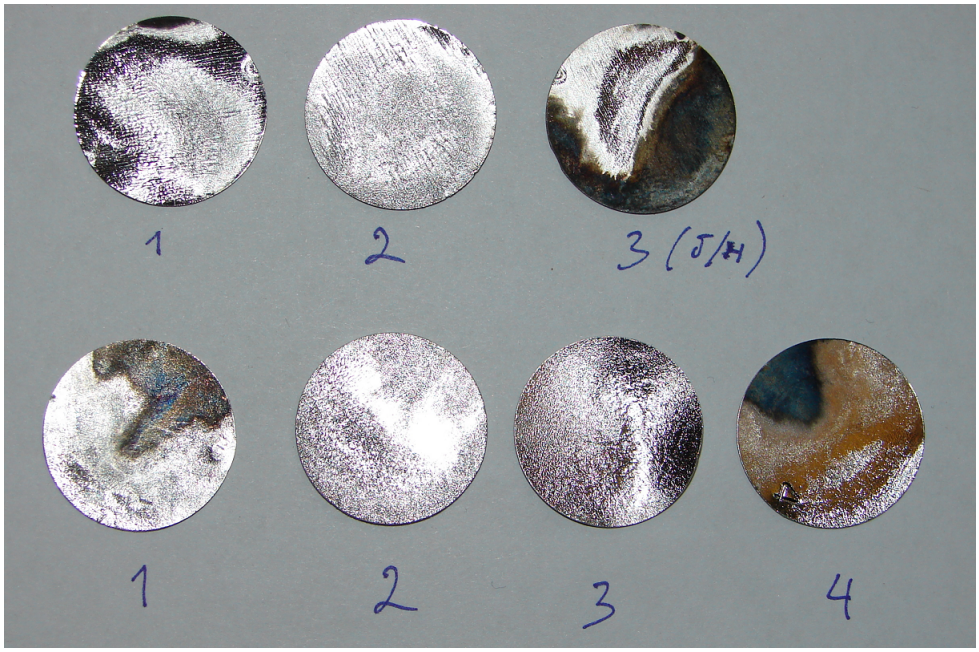

Figure 11: Image of the processed specimen, upper row is tungsten (W), lower row is steel

6 Modelling of the interaction and evaporation

As the motivation of the experimental work was to give fundamental data for the modelling of evaporation, the next step after the experiment is the modelling of the liquification and evaporation of steel and tungsten. For steel, a semi-empirical model exists, but comparison with other models could give new insights into the process, especially for high thermal loads. As mentioned before, for tungsten, no evaporation models for very high thermal loads and surface temperatures exist so far. Thus, the semi-empirical models are based on measurements results obtained at lower temperatures.

6.1 Heat Conduction

To describe the heat transfer inside of the sample without the influence of convection, we take the equation of the heat conduction without sources into account:

$$\rho(T)c_p(T)\frac{\partial T}{\partial t} - \nabla \cdot (\lambda(T)\nabla T) = 0 \tag{6.1}$$

with the density $\rho(T)$, the heat capacity $c_p(T)$ and the $\lambda(T)$. By the assumption of only one-dimensional heat flux in the dimension z and the thermal diffusivity $\alpha(T) = \frac{\lambda(T)}{c_p(T)\rho(T)}$ this leads to

$$\frac{\partial T}{\partial t} = \alpha(T)\frac{\partial^2 T}{\partial z^2} \tag{6.2}$$

It is very important to mention the high dependency of the thermal diffusivity α on the temperature, which is considered in detail in the chapter 6.1.1. For the surface, the temperature is in the following relation to the heat flux:

$$-\lambda\frac{\partial T}{\partial z} = \dot{q}(t) \tag{6.3}$$

The source term on the surface $\dot{q}(t)$ can be splitted to

$$\dot{q}(t) = \dot{q}_0(t) - \dot{q}_{evap} - \dot{q}_{rad}(t) - \dot{q}_{lost} \tag{6.4}$$

in a term of incoming heat from the plasma flow $\dot{q}_0(t)$, heat "lost" due to evaporation of the surface $\dot{q}_{evap}$ and heat emitted by radiation $\dot{q}_{rad}(t)$. This term can be expanded, describing also heat lost due to excitation and other occurring processes. The heat lost due to heating of the evaporated material is described by the term $\dot{q}_{lost} = \frac{\partial s}{\partial t}\rho c_p(T)T_s$.

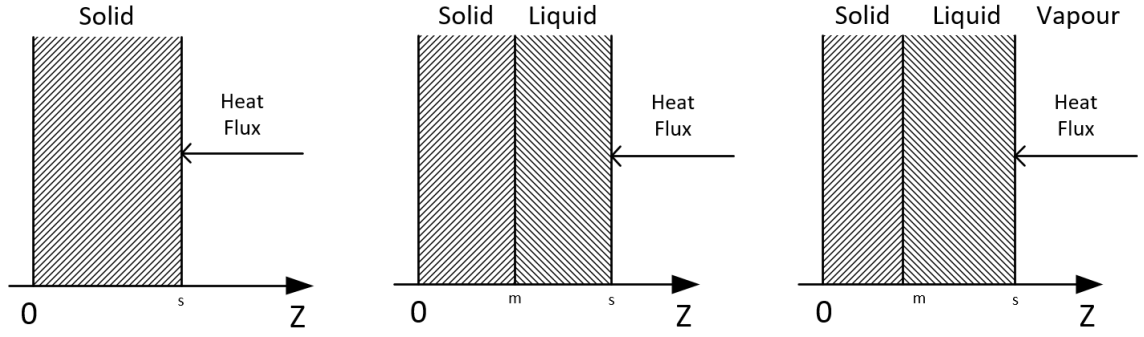

(a) Wall before appearance of the liquid phase, $0 < T < T_m$

(b) Wall after appearance of the liquid phase,$T_m < T < T_v$

(c) Wall after appearance of vapour, $T_v < T < T_f$

Figure 12: Process of vaporization [20]

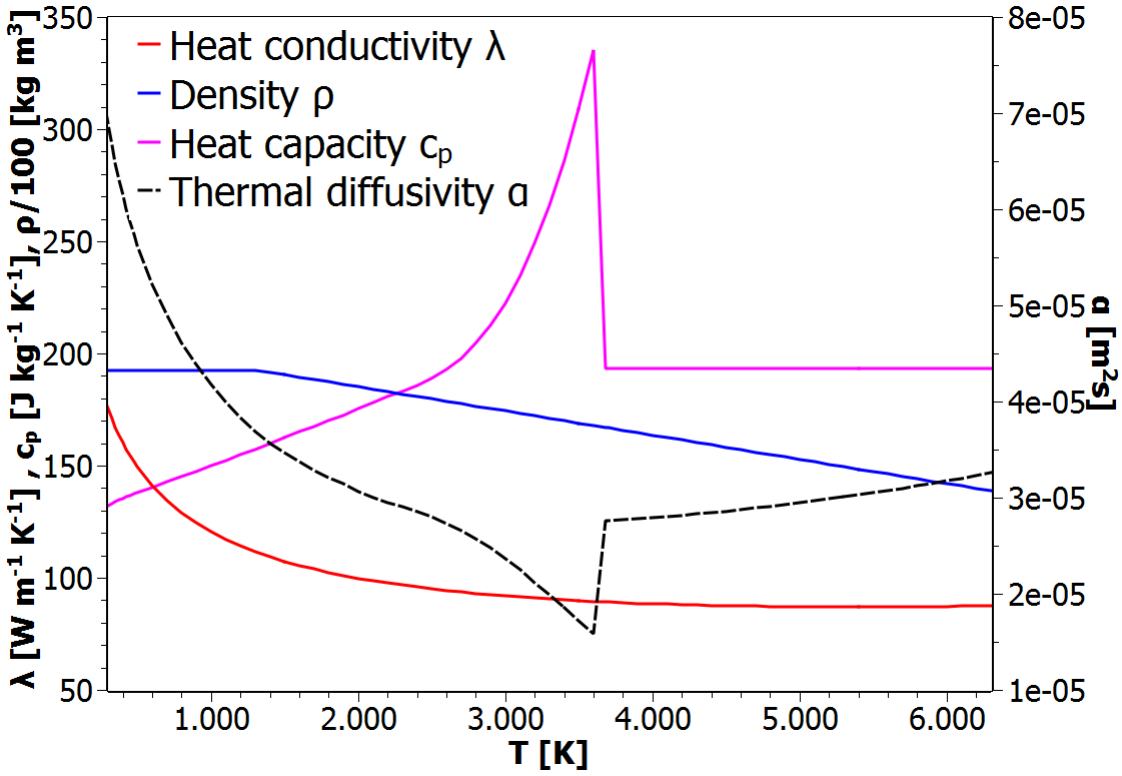

Figure 13: Heat conductivity λ [21], Density ρ [22], Heat capacity c_p [3] and thermal diffusivity α of tungsten as functions of temperature T

6.1.1 Thermodynamic properties of steel and tungsten

In figure 13 and figure 14, the heat capacity c_p, heat conductivity λ, density ρ and the directly dependent thermal diffusivity α of tungsten and steel are shown as functions of the temperature T. Especially the heat conductivity is highly influenced by the temperature and sinks drastically while coming close to the boiling point. The density of tungsten is given by the relation

$$\rho_W(T) = 16.7(\pm 0.33) \cdot 10^3 – 1.08(\pm 0.08)(T – T_m)\text{kg/m}^3 \tag{6.5}$$

with the melting point temperature $T_m = 3695$ K[22]. The density of steel as an alloy of iron and carbon with a percentage $pct = 2$ of carbon and and can be determined [24] by the relation

$$\rho_{Fe}(T) = ((7.1 - 0.0732pct) - (8.28 - 0.874pct) \cdot 10^{-4} \cdot (T - T_m)) \cdot 10^3 \text{kg/m}^3 \tag{6.6}$$

with the melting point $T_m = 1823$ K and standard temperature $T_0 = 298.15$ K. The thermal conductivity of tungsten as a function of the temperature is given by the corellation as a multi-linear regression of the form

$$\lambda(T) = aT^b e^{cT} e^{d/T} \tag{6.7}$$

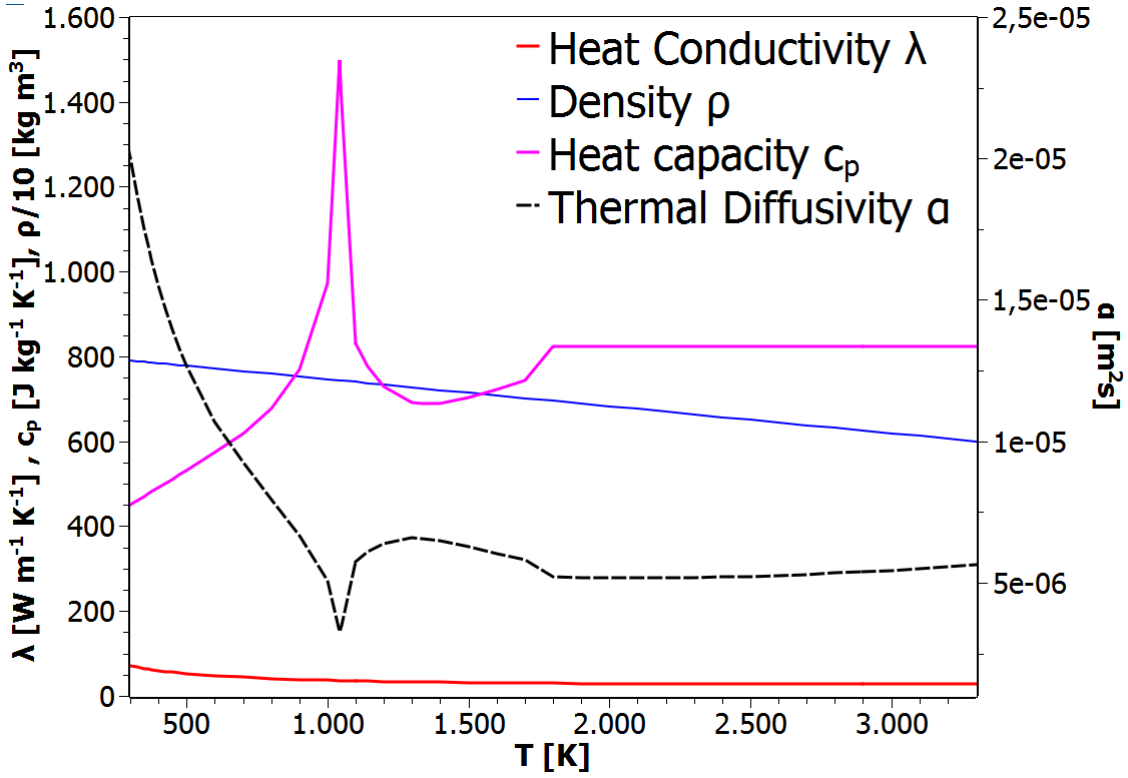

Figure 14: Heat conductivity λ [23], Density ρ [24], Heat capacity c_p [3] and thermal diffusivity α of steel as functions of temperature T

with the coefficients from [23] given in table 9. The correlation has also been validated by the thermal conductivity given in [21]. The heat capacity is given by the Shomate equation

$$c_p(T) = A + B\frac{T}{1000} + C(\frac{T}{1000})^2 + D(\frac{T}{1000})^3 + \frac{E}{(\frac{T}{1000})^2}, \tag{6.8}$$

which coefficients are given in table 8.

6.2 Evaporation

As the surface temperature due to the incoming heat flux rises, evaporation might occur. It is assumed, that the evaporation takes place as the process shown in figure 12. So in the first face, only the solid phase is heated, then a liquid phase appears due the surface temperature exceeding the melting temperature and then a measurable vapour phase occurs. Based on kinetic theory, also in the first two steps evaporation occurs, but in such a low amount, that it is not considered as relevant for our problem. The heat lost to the energy fed into the evaporation can

	T [K]	A	B ($\cdot 10^{-8}$)	C ($\cdot 10^{-9}$)	D ($\cdot 10^{-10}$)	E ($\cdot 10^{-9}$)
Fe [25]	1837-3273	46.02400	−1.884667	6.094750	−6.640301	−8.246121
W [21, 25]	298.15 - 6100	35.56404	−15.51741	29.15253	−189.1725	−410.7702

Table 8: Coefficients for the specific heat capacity c_p by the shomate equation 6.8

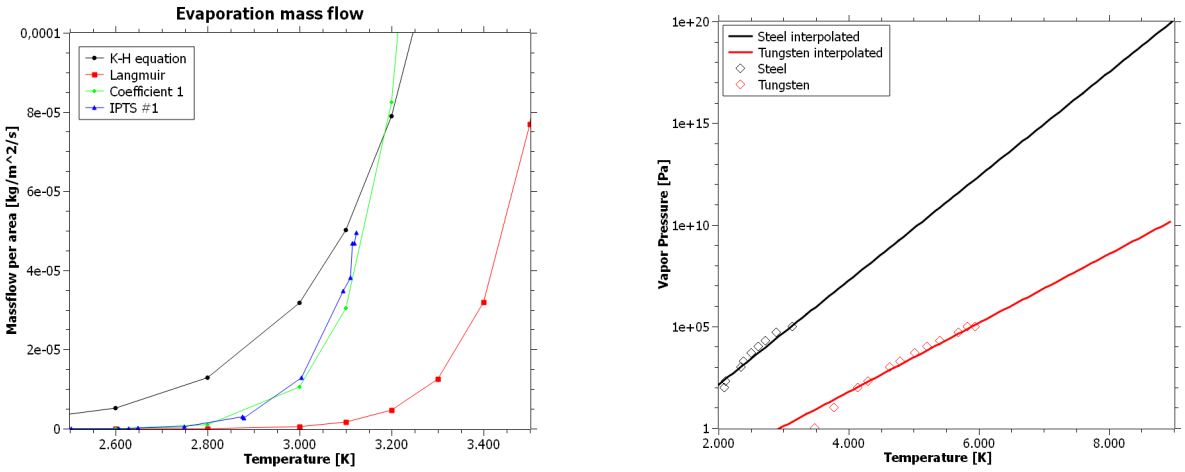

(a) Evaporation massflow of tungsten as a function of temperature. K-H equation has been calculated directly by the Knudsen equation 6.11, Langmuir is the results given in [4], and IPTS # 1 are measurement results by [6]. Coefficient 1 is calculated by equation 6.14 with the coefficient fitted to the data of IPTS # 1.

(b) Vapor pressures of tungsten and steel as a function of temperature, measurements (points) and exponential interpolation (lines)

Figure 15: Diagrams for evaporation massflow and vapor pressure

be calculated as

$$\dot{q}_{evap} = E_s \rho_s \left(\frac{\partial s}{\partial t} \right), \tag{6.9}$$

where E_s is the lattice energy, ρ_s is the vapor density. The speed of the boundary between liquid and vapor is given by the different evaporation models, but also in relation to the evaporation mass flow $\dot{m}$ and the density $\rho(T)$

$$\frac{\partial s}{\partial t} = \frac{\dot{m}}{\rho(T)} \tag{6.10}$$

6.2.1 Kinetic Approach

The mass evaporation rate $\dot{m}$ can be described by the Langmuir-Knudsen or Knudsen-Hertz (KH) equation [26], which is derived from kinetic gas theory:

$$\dot{m} = \frac{p_s}{\sqrt{2\pi MRT}} = \frac{(p_s - p_1)}{\sqrt{2\pi k T m_a}} = \sqrt{\frac{M}{2\pi RT}} p_s \tag{6.11}$$

In equation 6.11, T is the temperature, M is the molar mass, R is the gas constant, and m_a is the atomic mass. The parameter p_1 is the environmental pressure, for the calculations assumed as zero because of the surrounding vacuum. The vapor pressure p_s can be determined by

	a	b	d	d
Fe	2227.664	−0.627271	$2.09554 \cdot 10^{-4}$	22.35452
W	1675.621	−0.388818	$7.17926 \cdot 10^{-5}$	$-18,4985$

Table 9: Coefficients for the heat conductivity λ in equation 6.7

measurements and is interpolated by an exponential function, which results are shown in figure 15, where an exponential function was fitted onto the measurements given by [3]. The following exponential fits describe the vapour pressure

$$p_W(T) = 10^{-5} exp(0.0039T) \tag{6.12}$$

$$p_{Fe}(T) = 10^{-3} exp(0.0059T) \tag{6.13}$$

From this point it follows that the kinetic approach is directly dependent onto the calculation of the vapor pressure. As mentioned earlier the determination of the vapor pressure is not simple due to the high temperature, especially for tungsten. Thus, the accuracy of this model depends on the accuracy of the vapor pressure measurements. So a different approach might be useful.

6.2.2 Semi-empirical approach

Another approach to the problem, which follows directly from the prior model is to determine the mass flux without directly calculating the vapor pressure. Equations 6.11 and **??** can be combined to a simplified, Arrhenius-like form:

$$\dot{m} = A_1 T^{-0.5} exp(\frac{-E_s}{kT}), \tag{6.14}$$

with A_1 as an empirically determined constant, that can be evaluated by comparison with experimental measurements of the evaporation mass flow. This formulation can thus be called semi-empirical (SE). E_s is the lattice energy, which is in between 8 and 9 eV/atom. For iron alloys, in our case steel, the empirical constant is determined as $A_1 = 1.202 \cdot 10^{10}$ kg/m^{2}s [27]. From earlier measurments of the tungsten evaporation massflow [4, 6] the empircal constant $A_1 = 2 \cdot 10^{12}$ kg/m^{2}s was calculated. Results of the evaporation mass flow for the different calculation methods are shown in figure 15.

6.2.3 Formulation of the one-dimensional Stefan problem

The model for the liquification and evaporation of metal is a generalization of the Stefan problem [20]. For an inverse Stefan problem with a moving front, the interface speed v_e between the liquid and the vapor phase follows the relation [20]

$$\lambda \frac{\partial T}{\partial z} - \dot{q}(t) = L_v \rho v_e, \tag{6.15}$$

in which $\dot{q}(t)$ is the heat flux at the interface and L_v is the latent heat of vaporization, which is in between $774 - 805$ kJ mol^{-1} and around 354 kJ mol^{-1} for iron [1]. An advantage of this model is found by the fact that it does not rely on empirical values but on an purely mathematical approach. Thus it should be valid in all temperature regions and not only in areas covered by measurements. A very close mathematical formulation as given in equation 6.15 can be used to

determine the movement speed v_s of the liquid phase

$$\lambda_s\left(\frac{\partial T}{\partial z}\right)_s - \lambda_l\left(\frac{\partial T}{\partial z}\right)_l = L_m \rho(T) v_s \tag{6.16}$$

with λ_s and λ_l being the heat conductive of the solid and the liquid phase. L_m is the latent heat of melting, which is 35.4 $\mathrm{kJ\,mol^{-1}}$ for tungsten and 13.81 $\mathrm{kJ\,mol^{-1}}$ for iron.

6.3 Excitation, ionization and radiation of evaporated atoms

With high temperature, an estimation of the emitted radiation comes to interest. The heat flux due to radiation is calculated directly by

$$\dot{q}_{rad} = \sigma(T_s^4 - T_0^4). \tag{6.17}$$

It is obvious, that the radiation on the surface is dependent on the environment temperature T_0 and the surface temperature T_s, which is to determine by the simulation. σ is the Stefan-Boltzmann-constant. To examine how much energy is lost due to excitation and ionization of the metal sample, an approach of the kinetic gas theory [28] is used, to determine the ratio between excited and neutral aotms:

$$\frac{n^*}{n} = 1 - erfC^* + \frac{2}{\sqrt{\pi}} C^* e^{-C^{*2}} \tag{6.18}$$

with the assumption, that only atoms with the critical speed c^* have energy higher than the excitation or ionization energies E_e and E_i. The error function given in [28] is calculated by use of the ratio $C^* = \frac{c^*}{\sqrt{2kT/m_a}}$ This energies can have high influence onto the temperature of the vapour layer.

6.4 High temperature instabilities of the crystal lattice

At high temperatures, vibration of the crystal lattice can occur, leading to instabilities of the lattice and thus to destruction of the bonding. This leads to a higher progress of the solid to liquid phase transition inside of the sample and thus to a thicker liquid layer. In the liquid layer phenomena as temperature and mass transport by convection might appear. Due to this, the activation energy of the evaporation process can be drastically lowered [29, 30]. Still the modelling of this process is more sophisticated and might be reconsidered in further works. Also, for high temperatures, the lattice energy E_s goes to zero for $T_s \to T_{boil}$. This also leads to an increase of the evaporation rates, but the exact dependence of the lattice energy onto the temperature is hard to determine and only empirical approaches to determine it where used. It has also to be said, that the accuracy of only-emprical approaches might not be very high.

7 Numerical calculation of the evaporation and heat conduction

With the intention to compare the different options of modelling the evaporation with the experimental results, the use of a numerical algorithm which can resemble the different models is needed. A finite-differences algorithm with a moving boundary at the interface to the vapour phase seems suitable to solve the relevant equations given in chapter 6 and is also known as suitable for the problem [20, 31]. The area of calculation is approximated by an equidistant finite difference grid with N_z cells in space and N_t cells in time. For the boundary conditions, at each boundary one ghost cell is added. In figure 7, the grid with spatial dimension z, dimension in time t and indices is shown. For the marching in the spatial dimension z, the index j is used, for marching in time, the index i. Using the finite difference approximations introduced in chapter 3.5, equation 6.2 can be written as

$$\frac{1}{\Delta t}(T_{i+1,j} - T_{i,j}) = \alpha \frac{1}{\Delta z^2}(T_{i,j+1} - 2T_{i,j} + T_{i,j-1}), \tag{7.1}$$

where i is the index in time and j in space. This equation can be transformed into

$$T_{i+1,j} = T_{i,j} + \frac{\alpha \Delta t}{\Delta z^2}\big(T_{i,j+1} - 2T_{i,j} + T_{i,j-1}\big). \tag{7.2}$$

Thus equation 6.3 for the heat flux at the wall with the one-sided backward difference quotient 3.5 can be formed to:

$$T_{i,j-1} = T_{i,j} + \frac{\Delta z}{\lambda}\dot{q} \tag{7.3}$$

The assembly of $\dot{q}$ can be found in equation 6.4.
To resemble the very fast processes of evaporation accurately, very small steps in space and time have to be chosen, leading to a relatively fine grid. Otherwise, long-term development of the temperature distribution along the sample is also of interest, but leads to very high memory usage if such fine grids are used. This leads to different grids for time and space scales of interest. The time scale for the short-time simulation is usually around 50 µs, for the long term between 1 and 10 s. Also different space scales are used, as the skin depth for the evaporation problem only amounts up to 20-30% of the sample, but the full sample is of interest for the temperature distribution after long time. The different grids used are listed in table 10. A scheme of the used equidistant grid with the boundaries A and B is shown in figure 7. As seen in figure 7, the heatflux at the boundary A is described by the equation 7.3. Boundary B is an open border with

$$T_{i,j+1} = T_{i,j} \tag{7.4}$$

To resemble the evaporation of the material due to the high heat flux, the boundary A at $z = z(t)$ is considered as moving with the speed v_s obtained by equation 6.10.

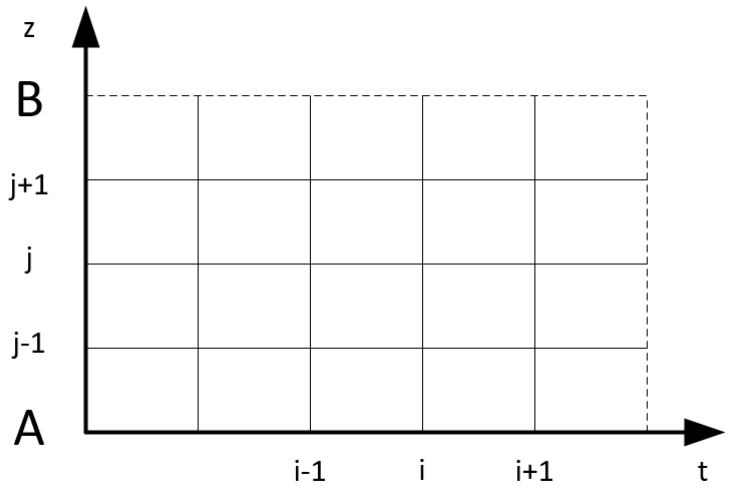

Figure 16: Finite difference grid with boundaries A and B

#	N_z	Nt	h [m]	t_{start} [s]	t_{end} [s]	Δz [m]	Δt [s]
1	800	40000	0.0002	$30 \cdot 10^{-6}$	$80 \cdot 10^{-6}$	$2.497 \cdot 10^{-7}$	$1.25 \cdot 10^{-9}$
2	1300	175000	0.0001	$3.3868 \cdot 10^{-5}$	$4.0882 \cdot 10^{-5}$	$7.6864 \cdot 10^{-8}$	$4.1259 \cdot 10^{-11}$
3	2000	100000	0.0001	$3.3868 \cdot 10^{-5}$	$3.91 \cdot 10^{-5}$	$4.997 \cdot 10^{-8}$	$6.012 \cdot 10^{-11}$
4	2000	100000	0.008	$3.3868 \cdot 10^{-5}$	$3.91 \cdot 10^{-5}$	$4.997 \cdot 10^{-8}$	$6.012 \cdot 10^{-11}$

Table 10: Mesh data used for simulation

7.1 Simulation of the short-time evaporation

From the temperature distribution $T(z,t)$ after time t the heat in the sample can be estimated by integration over the length

$$H = \rho \frac{\pi}{4} d^2 \int_0^h c_p(T) \cdot T(z,t) dz. \tag{7.5}$$

With insertion of $t = 0$ and $t = t_{end}$, the difference ΔH can be calculated, giving a possibility to compare the numerical results with the experimental data obtained in chapter 5. As the main focus of this work is the discussion of models for the evaporation of tungsten, the simulation results are discussed here first and the results for the evaporated mass and absorbed heat are listed in table 11.

The simulation of the evaporation with the former mentioned semi-empirical model and the meshes # 1 and # 2 leads to results for the surface temperature shown in figure 17. As it can be seen, the surface temperature is only partially dependent onto the incoming heat flux, reaching mostly 8000 K. Although the position of the boundary, which is shown in figure 18, changes dramatically with higher heat flux. This leads to the assumption, that for higher heat fluxes, as the material can not be heated far over the boiling point, more evaporation occurs. Still, the surface temperature is higher than the boiling point and rising with the incoming heat flux, as seen in figure 17. As the results for the evaporated mass and absorbed heat flux are in good

U_0	$\dot{q}_0$	$\Delta m_{sim,SE}$	$\Delta H_{sim,SE}$	$\Delta m_{sim,KH}$	$\Delta H_{sim,KH}$	$\Delta m_{sim,C}$	$\Delta H_{sim,C}$ [J]
5	$6.2382 \cdot 10^{11}$	0.0753	53	0.0751	84	0.0821	33.1
7	$1.1549 \cdot 10^{12}$	0.15853	100.77	0.147	94	0.1555	45.6
9	$1.8464 \cdot 10^{12}$	0.252	132.184	0.248	120	0.2651	105.39

Table 11: Evaporated mass Δm [µg] and absorbed heat ΔH [J] for simulations with the Knudsen-Hertz (KH) model, the semi-empirical (SE) model and the Stefan model (C), tungsten

agreement for the lower heat flux, the model seems valid for these temperature regions.
In figure 19, the surface temperatures for simulations with the Knudsen-Hertz model is shown. As it can be seen, the surface temperature is drastically lower as in simulations with the semi-empirical model. For all incoming heat fluxes, it is around 7000 K. Still, a change in boundary position and thus in the evaporated mass can be clearly seen in figure 20. The results for the evaporated masses are also in good agreement with the experimental data for the lower heat fluxes.
Finally, the results for simulations with the model by Stefan are shown in figure 21 for the temperature and in figure 22 for the boundary position. It can clearly be seen, that the behaviour of the surface temperature in simulations with this model is quite different. The surface temperature does have a much higher dependence onto the incoming heat flux than expected. Nevertheless, the boundary position and evaporated masses are in good agreement with the other models.
For steel, the results are different. The Stefan model gives no usable results and thus no simulation results are shown. It might not be stable due to the low melting and boiling points for steel resulting in a very high boundary speed. The results for the simulation with the Knudsen-Hertz model are shown in figure 23 for the boundary position and figure 24 for the surface temperature. Similar to the results from the tungsten simulations, a constant surface temperature of 3000 K independent from the incoming heat flux can be seen. Yet, the ablated mass is much smaller than expected from the measurements, for all heat fluxes. The same problem arises for the simulations with the semi-empirical model shown in figures 25 and 26. A constant surface temperature of 2500 K arises, but the ablated mass is far below the expected values. As the results for tungsten were sufficient, these problems may result from the model for steel. For steel the mesh # 3 was used. It can be seen for all simulation results, that oscillations of the surface temperature occur. These oscillations are typical for the direct finite-difference method and result due to the grid size, which steps are still too big to display the evaporation completely correct, as the change of the boundary for one time step Δt is smaller than the step Δz in space, following the relation

$$(\frac{\partial s}{\partial t}) \cdot \Delta t < \Delta z \tag{7.6}$$

Because of limited computational power, smaller step sizes where not possible. By repeating selected simulations with varying grid sizes, it was observed that the oscillations converge against their mean value, so the influence onto the final result is negligible.

U_0	$\dot{q}_0$	$\Delta m_{sim,SE}$	$\Delta H_{sim,SE}$	$\Delta m_{sim,KH}$	$\Delta H_{sim,KH}$
5	$6.2382 \cdot 10^{11}$	0.0528	22	0.048	20
7	$1.1549 \cdot 10^{12}$	0.098	33	0.088	31
9	$1.8464 \cdot 10^{12}$	0.161	35	0.157	34

Table 12: Evaporated mass and absorbed heat for simulations with the Knudsen-Hertz (KH) model, the semi-empirical (SE) model and the Stefan model (C), steel

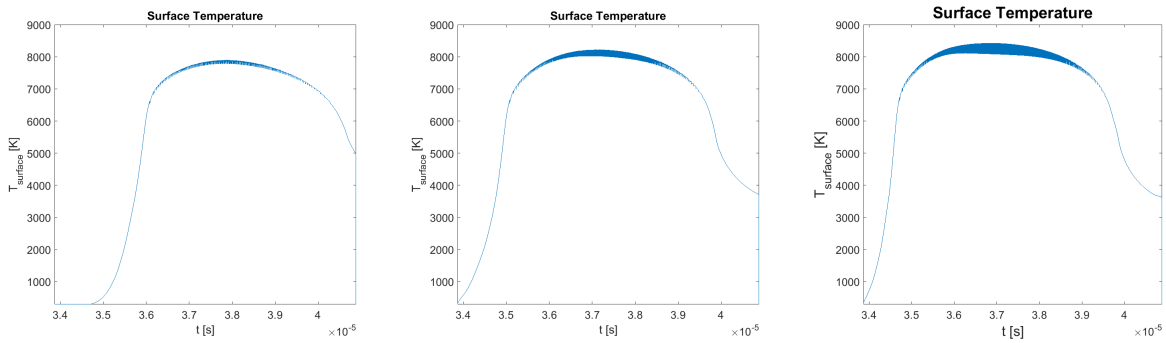

(a) 5kV discharge (b) 7kV discharge (c) 9kV discharge

Figure 17: Surface temperature from simulations for tungsten, Semi-Empirical (SE) model

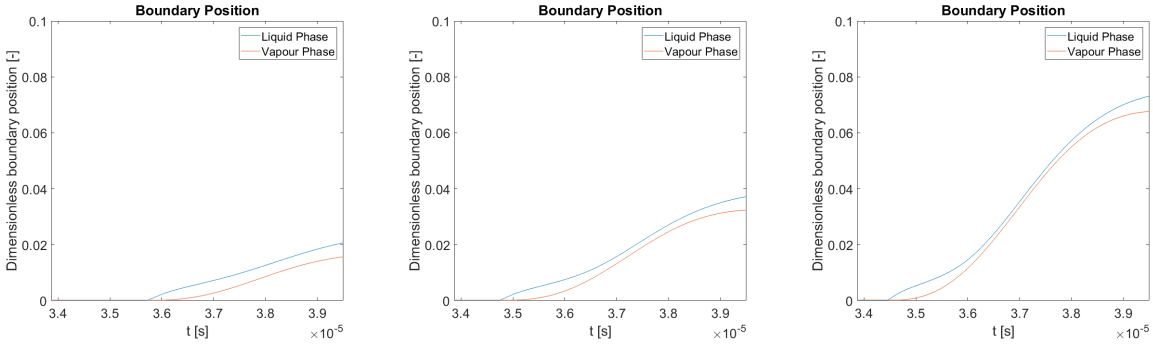

(a) 5kV discharge (b) 7kV discharge (c) 9kV discharge

Figure 18: Boundary position of the liquid and vapor phase from simulations for tungsten, Semi-Empirical (SE) model

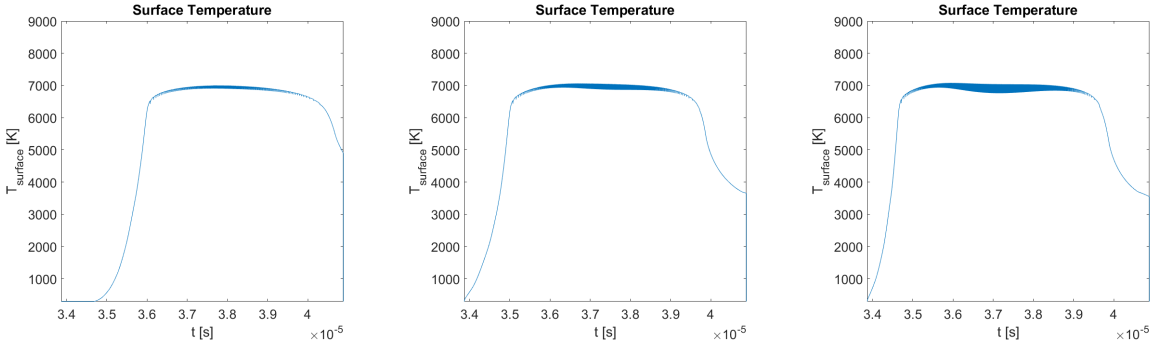

(a) 5kV discharge (b) 7kV discharge (c) 9kV discharge

Figure 19: Surface temperature from simulations for tungsten, Knudsen-Hertz (KH) model

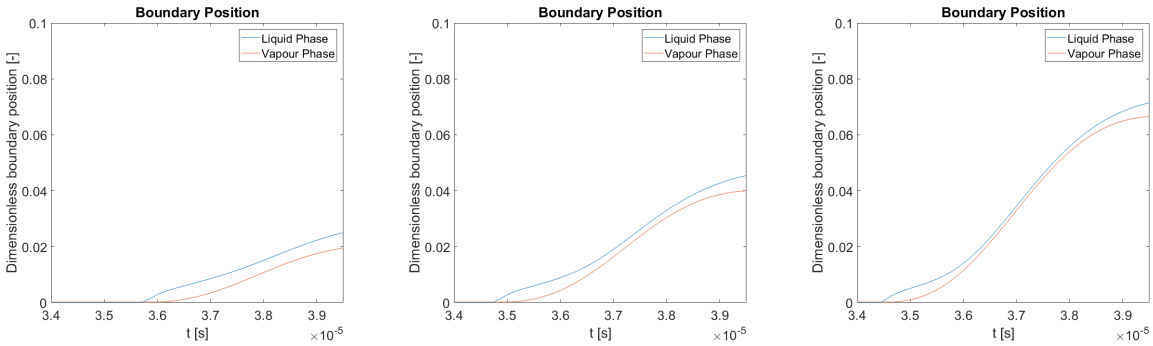

(a) 5kV discharge (b) 7kV discharge (c) 9kV discharge

Figure 20: Boundary position of the liquid and vapor phase from simulations for tungsten, Knudsen-Hertz (KH) model

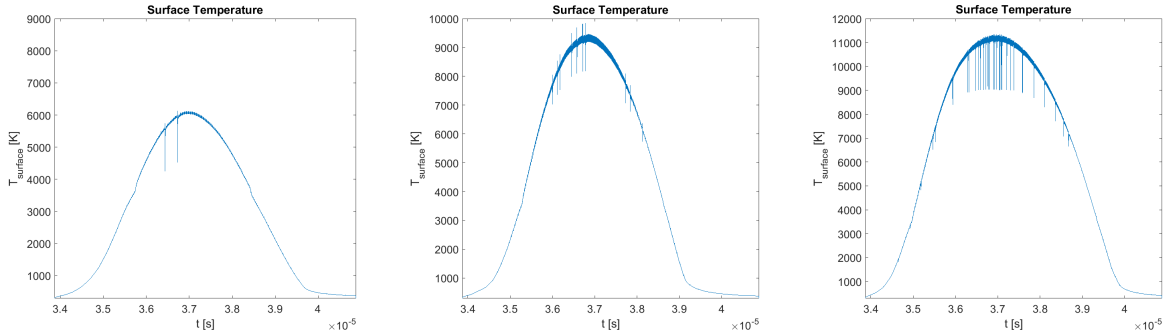

(a) 5kV discharge (b) 7kV discharge (c) 9kV discharge

Figure 21: Surface temperature from simulations for tungsten, Stefan model (C)

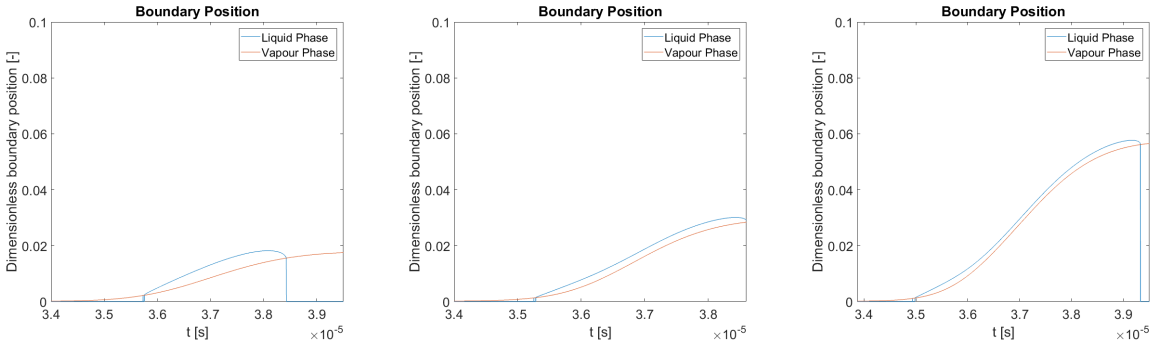

(a) 5kV discharge (b) 7kV discharge (c) 9kV discharge

Figure 22: Boundary position of the liquid and vapor phase from simulations for tungsten, Stefan model (C)

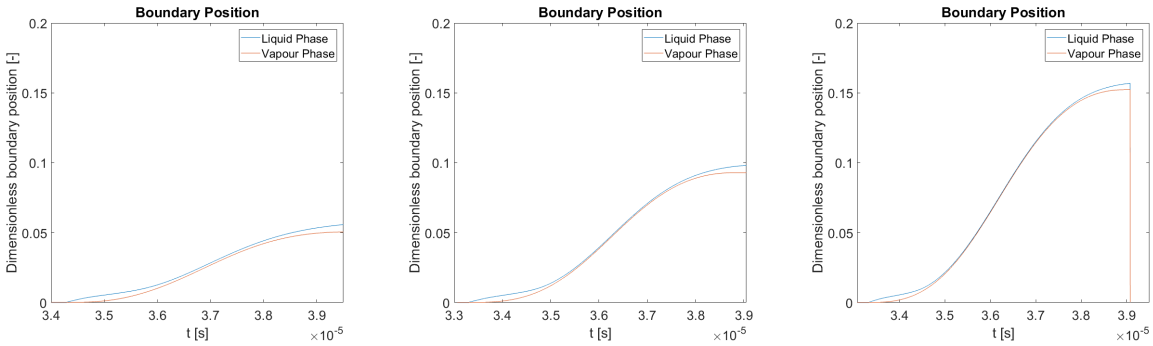

(a) 5kV discharge (b) 7kV discharge (c) 9kV discharge

Figure 23: Boundary position of the liquid and vapor phase from simulations for steel, Knudsen-Hertz model (KH)

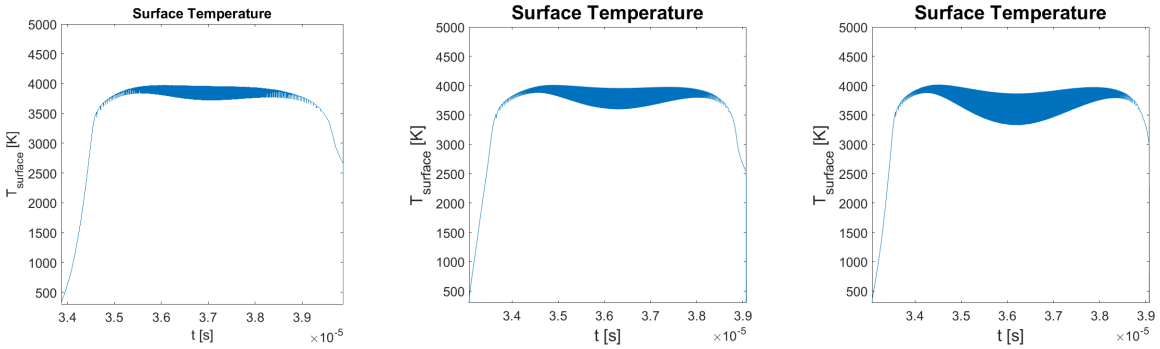

(a) 5kV discharge (b) 7kV discharge (c) 9kV discharge

Figure 24: Surface temperature from simulations for steel, Knudsen-Hertz (KH) model

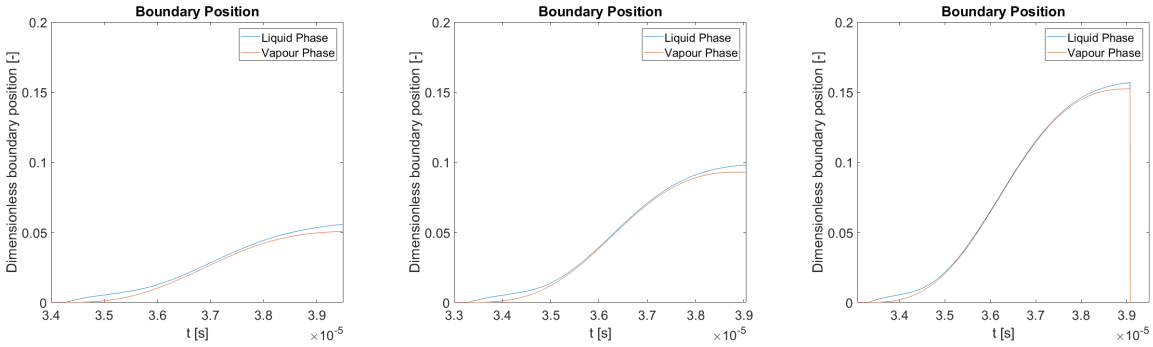

(a) 5kV discharge (b) 7kV discharge (c) 9kV discharge

Figure 25: Boundary position of the liquid and vapor phase from simulations for steel, semi-empirical model (SE)

U_0	$\Delta T_{sim,W}$	$\Delta t_{sim,W}$	$\Delta T_{exp,W}$	$\Delta t_{exp,W}$
5	36.631	0.006	31.4	10.4
7	77.95	0.006	83.9	12.8

Table 13: Temperature change of the sample after temperature equilibrium for tungsten in comparison to experimental values

7.2 Simulation of the long-time heat conduction

With the results of the short-time evaporation as a boundary condition, the heat conduction through the sample over a longer time period can be simulated. The results of this simulation can be directly compared to the measured temperatures from chapter 5, shown in figures 9 and 10. Due to the longer time-scale of this problem and the assumption that evaporation after this time is negligible, this part of the simulation can be realized with smaller grids, e.g. grid # 4 from table 10. The results can be found in table 13. In figure 27 it can be seen, that the temperature raise at the sensor side of the sample is much faster than in experiment. This may be a result of the slower heating of the thermocouple used for temperature measuerements and a delay due to the heat transfer between sensor and sample. Nevertheless, the temperature changes in the sample are in good agreement with the results form the simulations. The discrepancy of the results can be easily explained by the difference between the calculated absorbed heat and the measured absorbed heat. There have only been made simulations using the end condition of the semi-empirical model, which had the best agreement to the experimental results and only for discharge voltages of 5 kV and 7 kV due to the possibility to compare it with the measured temperature curves from chapter 5. Also the development of the temperature distribution over time is shown in figure 28. It can be seen, that the equilibrium over the whole sample is reached after $t = 0.006$ s. Summarizing, it can be said that the simulation results are in good agreement with the experimental measurements, although the slower heating of the sensor gives no direct possibility for comparison. For steel, because of the high discrepancy between experiment and simulation, no long-time simulations were done.

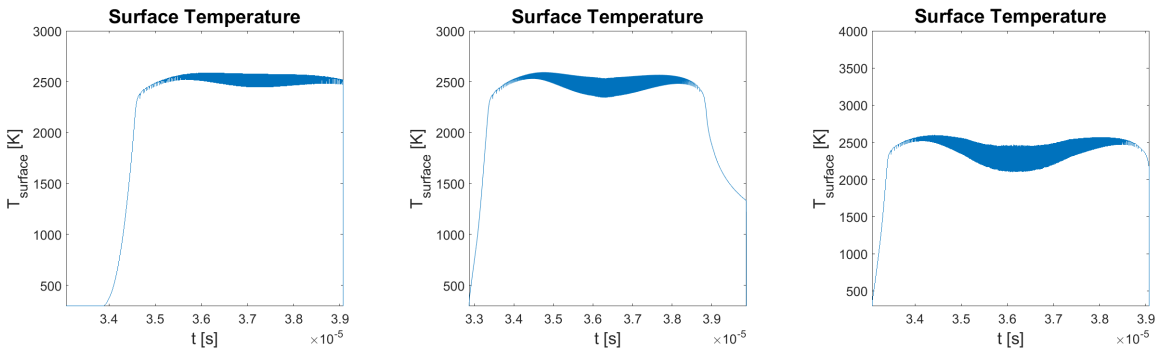

(a) 5kV discharge (b) 7kV discharge (c) 9kV discharge

Figure 26: Surface temperature from simulations for steel, semi-empirical (SE) model

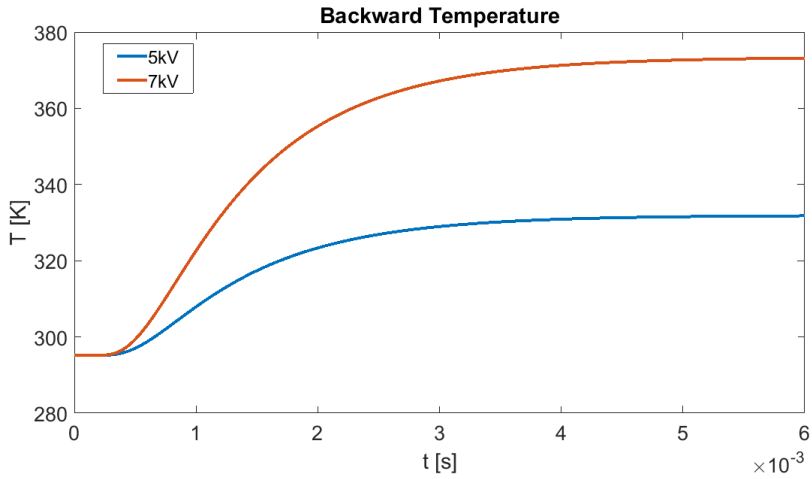

Figure 27: Temperature on the backside of the sample for 5kV and 7kV discharges with tungsten

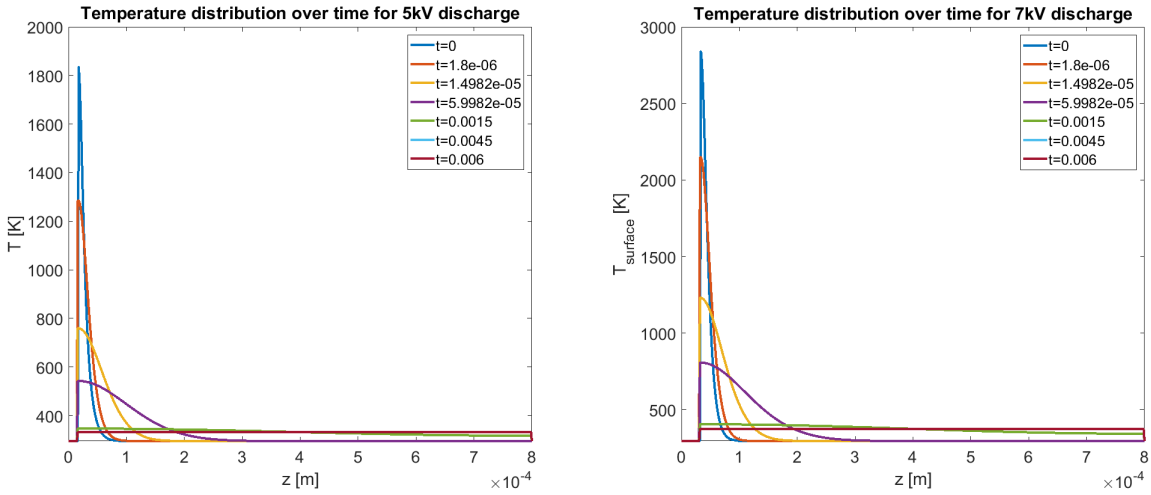

(a) 5kV discharge (b) 7kV discharge

Figure 28: Temperature distribution in the sample over time

8 Microscopical examination of specimen

To support the numerical analysis, images of the tungsten specimen have been taken by optical and electron microscopy. With the results of these images, the degradation of the materials after evaporation and sublimation can be examined. Also the surface structure is of interest to resemble the solidification process. With an optical microscope, images of the sample surface were taken. The images were only taken of tungsten samples for discharge currents of 7kV and 9kV and can be seen in figure 29. It is clearly visible, that the surface is unsteady, especially the 9kV sample. These cracks feed the assumption, that additional effects, not resembled by the models could apply. To further this assumptions, higher magnification could be usable. With electron microscopy, images of the tungsten samples with applied to discharges with 7 and 9 kV discharge voltages at higher magnification were taken. As it can clearly be seen, especially in figure 30b) and figure 31, cracks form on the surface. These cracks result from the very fast solidification of the liquid phase after heating, mainly due to the high heat gradient throughout the sample. Their influence on the long term durability of the material could be of interest of future work. The hughe crack size leads to a higher surface area for interaction with the flow and can also be considered as a 2-D unsteadiness leading to further effects onto the flow and the heat transfer. These effects could be catalysis at the wall and have such a high influence, that it is not negligible, as assumed earlier. Furthermore, the structure of the surface gives evidence, that evaporation took place due to the unsteadiness. Although it is an indication, that the evaporation may not be uniform over the sample. This was already assumed by the inspection of the specimen shown in figure 11. Still it gives more perspectives to improve the modelling of the evaporation.

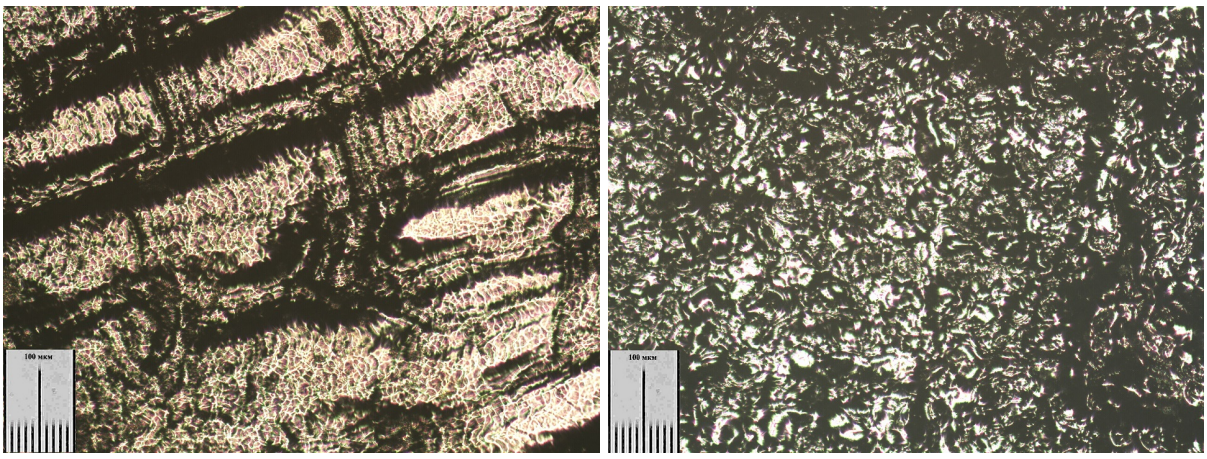

(a) 7kV wolfram specimen (b) 9kV wolfram specimen

Figure 29: Images of the wolfram specimen provided by optival microscopy, 100 times magnified

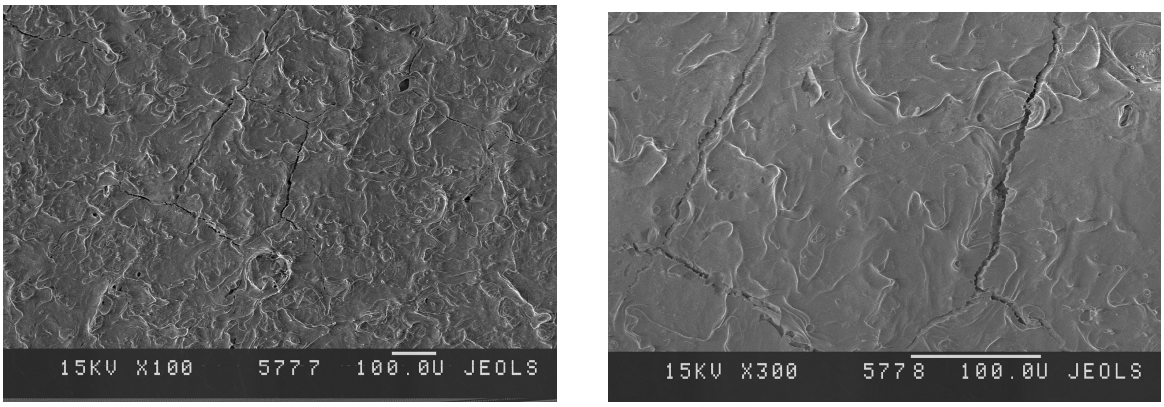

(a) 100 times magnified (b) 300 times magnified

Figure 30: Images of the 7kV wolfram specimen provided by electron microscopy

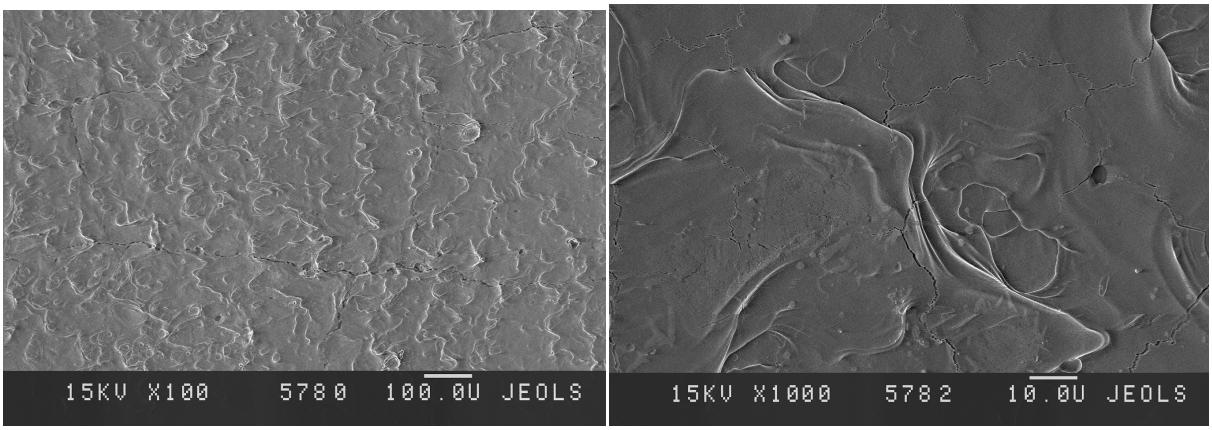

(a) 100 times magnified (b) 1000 times magnified

Figure 31: Images of the 9kV wolfram specimen provided by electron microscopy

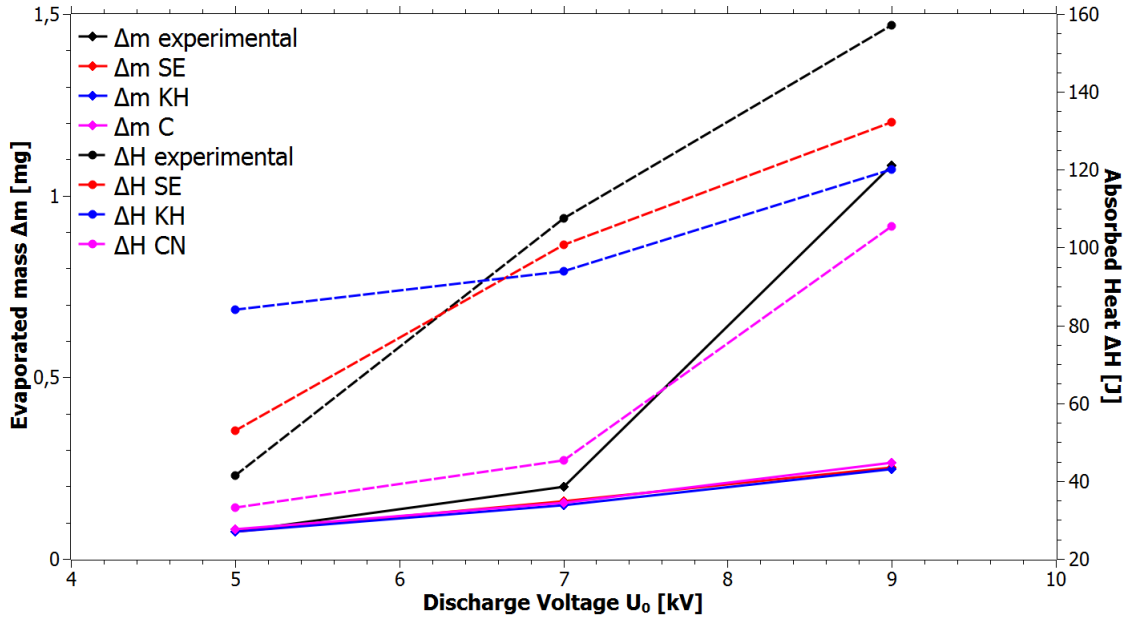

Figure 32: Comparison of ablated mass m and absorbed heat H for experimental results, and data calculated with Knudsen-Hertz (KH), semi-empirical (SE) model and Stefan (CN) model

9 Results of the analysis

Summing up the results of the experimental measurements and the numerical simulations, it has to said, that the results are ambiguous. The numerical analysis of the problem reveals some interesting effects: For all models used, the evaporated mass for the high discharge with $U_0 = 9$ kV is far below the experimental values. This can not only be due to computational errors, but may be a result of incomplete modeling. It has been found, that a lot of variables that take influence on the problem, don't have any clear values, as the physical properties of high temperature tungsten are not very well examined. It can clearly be seen in figure 32, that the congruence of the calculated evaporation mass with the experimental results is very high for lower heat fluxes regardless which model is choosen, and has also a very high difference for the high energy heat flux at a discharge voltage of $U_0 = 9$ kV. The surface temperature for different thermal loads is quite constant for the semi-empirical and the Knudsen-Hertz model, as over a specific temperature, the material is evaporated. This can be easily backed by the observation, that in simulations for tungsten, the temperature does not rise far above $T_s = 8000$ K, with a maximum of 8300 K for the simulations with the semi-empirical model, as seen in figure 17c). In the simulations with the Stefan model, the surface temperature was a dependant of the incoming heat flux. This might come from the different approach of the model. Still, all three models give good results for the 5 kV and 7 kV discharge for tungsten. The agreement with the experimental values is very high and validates the models for heat fluxes below 115.5 MW/cm^2. Especially the semi-empirical model gives a very good agreement both for evaporated mass and absorbed heat. Both other models have a more partial agreement, but still should be examined further, as other approaches still might be helpful for the problem. The influence of the radiation

onto the process is not very high, as for a surface temperature of 8000 K, the peak heat flux due to radiation as described by equation 6.17 is $q_{rad,max} = 1.37 \cdot 10^{10}$ W/m^2 for tungsten and $q_{rad,max} = 2.71 \cdot 10^8$ W/m^2 for steel. Therefore, for tungsten the heat flux due to radiation of the sample makes up $0.75-2\%$ of the incoming heat flux and $0.015-0.4$ % for steel, respectively. It can be reasoned, that it does not contribute much to the energy balance of the sample. Loss due to excitation and ionization is also very low, with the method described in chapter 6.3 it can be shown that for tungsten 99.57 % of the atoms are excited due to it's low excitation energy, but only 0.00495 % of the atoms are ionized. An explanation for the high difference between model and experiment for very high heat fluxes can be given by in multiple ways. First choice would be the rise of a convective term in the liquid layer which leads to higher mass transport. This assumption is hard to proof, but a first estimation can be given by calculation of the Nusselt number for the liquid layer, which is the proportion between convective and conductive heat transport:

$$Nu = \frac{hl}{\lambda} \tag{9.1}$$

For a global Nusselt number, the thermal conductivity $\lambda(T_m) = 89.1365$ is assumed to be constant over the liquid phase, while for the characteristic length l the hydraulic diameter, which is the diameter of the sample . The heat transfer coefficient is defined by $h = \frac{\dot{q}}{\Delta T}$, where $\dot{q}$ is the heat flux at the wall after evaporation as defined in equation 6.4 and $\Delta T = T_s - T_m$ is the gradient of the temperature between the boundary to the solid phase, where $T = T_m$ is the melting point and the surface temperature T_s. In table 14 the results of this calculations can be found. It is observed, that for the 9 kV discharge the Nusselt number rises to 0.6. This means, that the convective term makes up 60% of the heat transfer. It might not completely dominate the heat transport inside of the sample, but still be big enough to have an influence. For lower heat fluxes, the Nusselt number is lower, as expected. Still, this is only a very simple way to describe the heat transfer inside of the sample. Another possibility for the difference might be 2-D effects on the surface which are not represented by both the models and the simulation, as they are both one-dimensional. The observations of the surface made in chapter 8 give evidence, that the two-dimensional processes on the surface might have an effect. For the lower heat fluxes, this effect might only be smaller and such lead to the good agreement of the experiments and the simulation. The last explanation for the difference might be a measurement error for the ablated mass at the 9 kV discharge, especially as the absorbed heat is in good agreement with the simulation.

The error of the models for steel evaporation, as seen in figure 33, is systematically and might be reasoned by the very small empirical base for such models. Also, the Stefan model was not stable with steel. This might be due to its much lower melting and boiling point in combination with the very high heat fluxes. Also here, the rise of a convective term could be a reason for the difference, in addition to the materials much lower high temperature resistance. Similiar problems raised while modelling the tungsten evaporation, which leads to the assumption, that the big difference also is a result of a modelling problem, that could not be solved yet.

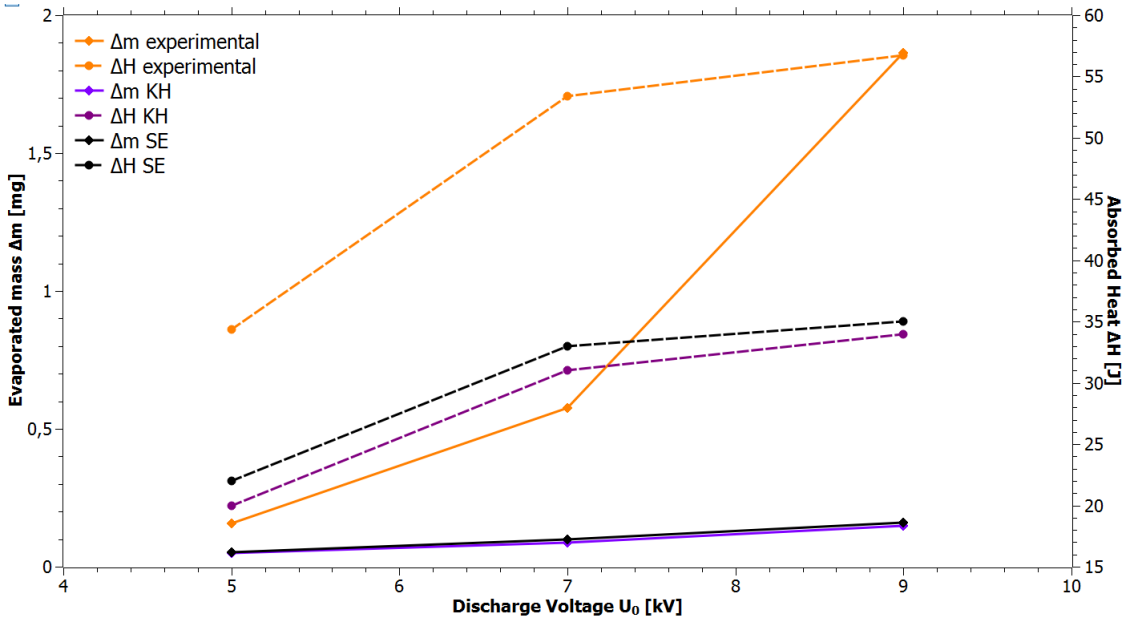

Figure 33: Comparison of ablated mass Δm and absorbed heat ΔH for experimental results and data calculated with Knudsen-Hertz (KH) and semi-empirical (SE) model, steel

U_0	$\dot{q}_{0,max}$ [W/m^2]	$\dot{q}_{max}$ [W/m^2]	T_s [K]	ΔT [K]	h	l [m]	Nu [-]
5	$6.2382 \cdot 10^{11}$	$1.89 \cdot 10^{11}$	8000	4305	$4.39 \cdot 10^{7}$	$4.458 \cdot 10^{-7}$	0.21
7	$1.1549 \cdot 10^{12}$	$4.023 \cdot 10^{11}$	8422	4727	$8.51 \cdot 10^{7}$	$3.46 \cdot 10^{-7}$	0.33
9	$1.8464 \cdot 10^{12}$	$7.2945 \cdot 10^{11}$	8763	5068	$1.4393 \cdot 10^{8}$	$3.69 \cdot 10^{-7}$	0.6

Table 14: Calculation of the Nusselt number for tungsten with the semi-empirical (SE) model

10 Conclusion

Summarizing this work, it has been found that the models do not reflect the evaporation of the tungsten completely, and for steel not even partially. It can be assumed, that there are additional terms in the formulation, which only take effect for very high heat fluxes. These could include a rising convective heat flux in the liquid phase which is driven by the high gradient between surface and the boundary between solid and liquid phase. As a result, the vapour pressure at the surface could be higher as assumed in earlier measurements, leading to a higher evaporation rate. Still it can be said, that the models for tungsten give quite good results for heat fluxes which are not too high, but additional terms have to be revisited for higher energies. As the main focus of this work was the model for tungsten, it can be said, that the results are sufficient, although the modelling of steel evaporation has to be revisited. For steel, also no known measurements of the evaporation rate for very high heat fluxes exist except [27], so the empirical base is very low. Further measurements of steel and tungsten evaporation, especially measurements of the surface temperature by pyrometry might give a huge insight into the process and help to expand the modelling of tungsten evaporation.
In addition, a improvement of the numerical algorithms used is urgent. The direct finite difference method shows some problems in dealing with the moving boundary and leads to oscillations.

A indirect finite difference method with a higher order might be sufficient but also a different method, e.g. finite volume, might be more suitable for this problem. Especially for the Stefan model a method more focused on the boundary movement of the liquid and vapour phase would be beneficial. It might also be possible to derive an analytical solution of the problem under the given assumptions and by reviewing the analytical methods given in [20].
Finally it can be said, that at least the experimental measurements were very successful, especially because no other measurements in this temperature region have been done yet. Further work in this field can be based on this measurements and those for low temperature regions[4]. The modelling is still in a very early phase, but at least for tungsten it showed some promising results. Furthermore, the results of this work also motivate further research in this topic of material science.

References

[1] Yiming Zhang, Julian R. G. Evans, and Shoufeng Yang. Corrected Values for Boiling Points and Enthalpies of Vaporization of Elements in Handbooks. *Journal of Chemical & Engineering Data*, 56(2):328–337, 2011. doi: 10.1021/je1011086. URL `http://dx.doi.org/10.1021/je1011086`.

[2] J.D. Cox, DD. Wagman, and V.A. Medvedev. *CODATA Key Values for Thermodynamics*. Hemisphere Publishing Corp., New York, USA, 1989.

[3] David R. Lide, editor. *CRC Handbook of Chemistry and Physics*. CRC Press, Boca Raton, FL, 84 edition, 2003.

[4] Irving Langmuir. The Vapor Pressure of Metallic Tungsten. *Phys. Rev.*, 2:329, 1913.

[5] Irving Langmuir. Vapor pressures, evaporation, condensation and adsorption. *J. Am. Chem. Soc.*, 54(7):2798–2832, July 1932.

[6] R. Szwarc, E. R. Plante, and J. J. Diamond. Vapor Pressure and Heat of Sublimation of Tungsten. *J Res Natl Inst Stan*, 69A(5):417, May 1965. doi: 10.6028/jres.069A.044.

[7] R. L. Burton and P.J Turchi. Pulsed Plasma Thruster. *Journal of Propulsion and Power*, 14(5):716–735, 1998. doi: http://dx.doi.org/10.2514/2.5334.

[8] Nickolay N. Antropov, Garry A. Popov, and Michael N. Kazeev. Ablative Pulsed Plasma Thrusters R&D in Russia since the Beginning of the 90s. Washington, D.C., USA, 2013.

[9] Michael N. Kazeev and Vladimir F. Kozlov. Ablation-Fed Discharge Characteristics. Ann Arbor, Michigan, USA, 2009.

[10] Yuri A. Alexeev, Michael N. Kazeev, and Vladimir F. Kozlov. Energy Transfer to the Propellant in High Power PPT. In *Proceedings of the 4th International Spacecraft Propulsion Conference*, Chia Laguna (Cagliari), Sardinia, Italy, 2004.

[11] Henri P. Wagner and Monika Auweter-Kurtz. Slug Model and Snowplow Model for Pulsed Plasma Thruster Description. Fort Lauderdale, Florida, July 2004.

[12] Henri P. Wagner and Monika Auweter-Kurtz. Plasma impulse based peening and decoating of engine parts and pulsed plasma thrusters for small spacecraft propulsion. *Vacuum*, 73(3): 461 – 467, 2004. ISSN 0042-207X. doi: http://dx.doi.org/10.1016/j.vacuum.2003.12.101. URL `http://www.sciencedirect.com/science/article/pii/S0042207X03002999`.

[13] Georg Herdrich, Markus Fertig, Stefan Kraus, Stefan Löhle, and Monika Auweter-Kurtz. Operational behavior and application regime assessment of the magnetic acceleration plasma facility IMAX. *Vacuum*, 85:563–568, 2010. doi: 10.1016/j.vacuum.2010.08.012.

[14] JAFAR SAFARIAN and THORVALD A. ENGH. Vacuum Evaporation of Pure Metals. *T.A. Metall and Mat Trans A*, (44):747, 2013. doi: doi:10.1007/s11661-012-1464-2.

[15] Clayton T. Crowe, Martin Sommerfeld, and Tsuji Yukata. *Multiphase flows with droplets and particles*. CRC Press, Boca Raton, FL, 2 edition, 2012.

[16] Michael N. Kazeev, Vladimir F. Kozlov, and Yuri S. Tolstov. High Power Plasma Flow Interaction with Micro- and Nanopowders. Wiesbaden, Germany, 2011.

[17] Claus-Dieter Munz and Thomas Westermann. *Numerische Behandlung gewöhnlicher und partieller Differentialgleichungen*. Springer Vieweg, Berlin, 3 edition, 2012.

[18] W. Rogowski and W. Steinhaus. Die Messung der magnetischen Spannung. *Archiv für Elektrotechnik*, 1(4):141–150, 1912. ISSN 1432-0487. doi: 10.1007/BF01656479. URL http://dx.doi.org/10.1007/BF01656479.

[19] D. A. Ward and J. La T. Exon. Using Rogowski coils for transient current measurements. *Engineering Science and Education Journal*, pages 105 – 113, 1993.

[20] John Crank. *Free and Moving Boundary Problems*. Clarendon Press, Oxford, 1 edition, 1984.

[21] Erik Lassner and Wolf-Dieter Schubert. *Tungsten : properties, chemistry, technology of the elements, alloys, and chemical compounds / Erik Lassner and Wolf-Dieter Schubert*. Kluwer Academic, New York, USA, 1999. ISBN 0-306-45053-4.

[22] Paul-François Paradis, Takehiko Ishikawa, Ryuichi Fujii, and Shinichi Yoda. Thermophysical properties of molten tungsten measured with an electrostatic levitator. *Heat Transfer—Asian Research*, 35(2):152–164, 2006. ISSN 1523-1496. doi: 10.1002/htj.20101. URL http://dx.doi.org/10.1002/htj.20101.

[23] S. I. Abu-Eishah. Correlations for the Thermal Conductivity of Metals as a Function of Temperature. *International Journal of Thermophysics*, 22(6):1855–1886, 2001.

[24] I. Jimbo and A. W. Cramb. The density of liquid iron-carbon alloys. *Metallurgical Transactions B*, 24(1):5–10, 1993. ISSN 1543-1916. doi: 10.1007/BF02657866. URL http://dx.doi.org/10.1007/BF02657866.

[25] NIST Chemistry Webbook, 2014. URL http://webbook.nist.gov/cgi/inchi/InChI%3D1S/Ar.

[26] Irving Langmuir. The Vapor Pressure of Metallic Tungsten. *Phys. Rev.*, 2(5):329–342, November 1913. doi: 10.1103/PhysRev.2.329. URL http://link.aps.org/doi/10.1103/PhysRev.2.329.

[27] P. N. Smith and R. G. Ward. The Evaporation of Liquid Iron Alloys Under Vacuum. *Canadian Metallurgical Quarterly*, 5(2):77–92, 1966. doi: 10.1179/cmq.1966.5.2.77. URL http://dx.doi.org/10.1179/cmq.1966.5.2.77.

[28] Arnold Frohn. *Einführung in die kinetische Gastheorie*. AULA-Verlag GmbH, Wiesbaden, 2. edition, 1988.

[29] Göran Grimvall, Blanka Magyari-Köpe, Vidvuds Ozolins, and Kristin A. Persson. Lattice instabilities in metallic elements. *Rev. Mod. Phys.*, 84(2):945–986, June 2012. doi: 10.1103/RevModPhys.84.945. URL http://link.aps.org/doi/10.1103/RevModPhys.84.945.

[30] V. Ozolins. First-Principles Calculations of Free Energies of Unstable Phases: The Case of fcc W. *Phys. Rev. Lett.*, 102(6): 065702, February 2009. doi: 10.1103/PhysRevLett.102.065702. URL http://link.aps.org/doi/10.1103/PhysRevLett.102.065702.

[31] E. Javierre, C. Vuik, F. J. Vermolen, and S. van der Zwaag. A comparison of numerical models for one-dimensional Stefan problems. *Journal of Computational and Applied Mathematics*, 192(2):445 – 459, 2006. ISSN 0377-0427. doi: http://dx.doi.org/10.1016/j.cam.2005.04.062. URL http://www.sciencedirect.com/science/article/pii/S0377042705003730.

List of Figures

Hiermit erkläre ich, dass ich die vorliegenden Arbeit nur mit den angegebenen Hilfsmitteln ohne unerlaubte fremde Hilfe selbstständig angefertigt und verfasst habe.

Stuttgart, Juni 2017
Jens Schmidt